Available online at www.sciencedirect.com
ScienceDirect
Comput. Methods Appl. Mech. Engrg. 336 (2018) 444–470
Computer methods in applied mechanics and engineering
www.elsevier.com/locate/cma

A fully coupled finite element formulation for liquid–solid–gas thermo-fluid flow with melting and solidification

J. Yan, W. Yan, S. Lin, G.J. Wagner*

Department of Mechanical Engineering, Northwestern University, United States

Received 2 September 2017; received in revised form 23 February 2018; accepted 12 March 2018
Available online 20 March 2018

Abstract

Many important industrial processes, such as additive manufacturing, involve rapid mass, flow and heat transport between gas, liquid and solid phases. Various associated challenges, such as the large density ratio between gas and condensed phases, make accurate, robust thermal multi-phase flow simulations of these processes very difficult. In order to address some of the associated challenges, a computational framework for thermal multi-phase flows is developed based on the finite element method (FEM). A unified model for thermal multi-phase flows similar to the models widely used in the manufacturing community is adopted. The combination of the level-set method and residual-based variational multi-scale formulation (RBVMS) is used to solve the governing equations of thermal multi-phase flows. Phase transitions between solid and liquid phases, i.e., melting and solidification, are considered. Interfacial forces, including surface tension and Marangoni stress, are taken into account and handled by a density-scaled continuum surface force model. A robust fully coupled solution strategy is adopted to handle various numerical difficulties associated with thermal multi-phase flow simulations, and implemented by means of a matrix-free technique using Flexible GMRES. The mathematical formulation and its algorithmic implementation are described in detail. Four numerical test cases are presented to demonstrate the capability of the proposed formulation. The first case is a benchmark example of solidification of aluminum in a graphite mold, the second case is a thermo-capillary droplet migration problem, the third case is a spot laser melting problem, and the fourth case is the melting of metal with an interior gas bubble. The computational results are compared with analytical, experimental and simulation data from other researchers, with good agreement in cases where such data is available.

Keywords: Thermal multi-phase flows; Gas–liquid–solid systems; Surface tension; Marangoni stress; Melting; Manufacturing

1. Introduction

Thermal multi-phase flows occur in many traditional manufacturing processes, such as welding and casting, as well as additive manufacturing processes, such as selective laser melting [1–5]. Although there are several numerical methods available for the simulations of single phase thermal fluid flows in the literature [6–11], accurate simulation

* Corresponding author.
E-mail address: gregory.wagner@northwestern.edu (G.J. Wagner).

https://doi.org/10.1016/j.cma.2018.03.017
0045-7825/

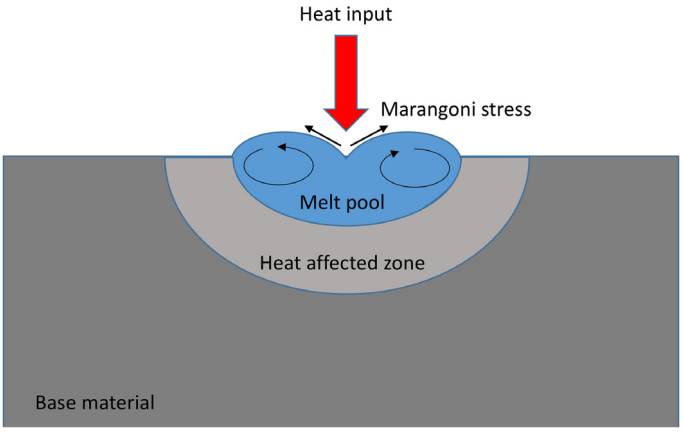

Fig. 1. A 2-D sketch of the melting process, showing the melting pool and the heat affected zone.

and solution strategies of these thermal multi-phase flows that can capture complex multi-physical phenomena in manufacturing processes with large property ratios, still remain a challenging problem.

From the pure fluid mechanics side, the challenges stem from the large density and viscosity ratios between different phases of fluid, pressure discontinuity across the interface, topological interface change, and effects of surface tension and its dependence on temperature. The last of these becomes significantly important for small spatial scales and in the presence of highly curved interfaces and large temperature gradients. In recent decades, a number of techniques have been developed to simulate isothermal multi-phase flow problems. These can be classified into two categories based on how the motion of the interface between different phases is handled: interface-tracking and interface-capturing methods [12,13]. The interface-tracking approaches, including front-tracking methods [14], boundary-integral methods [15], arbitrary Lagrangian–Eulerian (ALE) methods [16], and space–time finite-element methods [17,18], use a deformable mesh that conforms to the moving interface. The main advantage of interface-tracking methods is their ability to achieve high per-degree-of-freedom accuracy near the interfaces. However, when the interfaces form a singularity or change topology, interface-tracking methods become challenging to apply in practice, and require the development of special techniques (see, e.g., [19]). Automatic merging or break-up of interfaces are especially challenging for interface-tracking techniques, which makes 3D multi-phase flow problems notoriously more difficult to solve using this class of methods. On the other hand, interface-capturing methods, such as the volume-of-fluid (VOF) method [20], phase-field methods [21–25], diffuse-interface methods [26,27], front-capturing methods [28], and level set methods [29–33], utilize an auxiliary function defined on the problem domain to describe the interface, and present a practically simpler alternative to the interface-tracking methods. Although interface-capturing methods typically require higher mesh resolution to compensate for lower interface accuracy, these methods are very robust and relatively simple to implement in practice. Because the changes in interface topology do not present a conceptual difficulty for these methods, they have been applied to a broad range of problems including bubble dynamics [34–36], jet atomization [37], and free-surface flows [38–41]. Among these methods, the level set technique is especially popular because of its ability to represent complex interfaces using a smooth implicit function. In principle, this function can be used not only to separate the different fluid phases at their interface, but also to compute the interface normal and curvature that are needed to incorporate the interfacial forces, such as surface tension, in the multi-phase flow model.

As discussed above, great progress has been made in single phase thermal fluid flow and isothermal multi-phase flow simulations in recent years. However thermal multi-phase flows simulations for manufacturing processes are still very difficult. The coupling between thermodynamics and fluid dynamics increases the complexity of thermal multi-phase flow simulations as it involves the interplay of aspects, such as flow, mass, and heat transport, melting, solidification, and interface deformation. These interacting phenomena are illustrated by a typical melting problem shown in Fig. 1. In Fig. 1, a non-uniform heat influx (e.g. from a laser source) melts the solid workpiece into a liquid pool and creates a thermal gradient at the free surface. The dependence of surface tension on temperature gradient thus results in a significant spatial variation of surface tension, manifested in Marangoni stresses at the free surface,

which in turn drive liquid flow in the melt pool. This Marangoni-driven flow can have a profound impact on heat transfer in the melt pool as well as the shape of the melt pool.

In this paper, we aim to provide a robust and stable thermal multi-phase flow simulation tool for manufacturing processes with complex geometry. Such capability is highly desirable but still lacking in the industrial and academic communities. We propose a FEM-based computational multi-phase flows formulation to model the complex gas–liquid–solid systems with large property ratios between different phases. The governing equations are based on a unified model for thermal fluid/solid flows, which is similar to models widely used in the manufacturing community for welding, casting, and additive manufacturing [4,5,42–48].

The level set method is adopted in our model to distinguish the gas and condensed phases. The residual-based variational multiscale (RBVMS) formulation [49] is employed to solve the coupled Navier–Stokes, level set convection and energy conservation equations. RBVMS, as one of the key techniques in the formulation, was proposed in [49] for the simulation of incompressible turbulent flows. Since then, several research contributions [50–58] have shown that RBVMS yields accurate solutions on meshes with large-eddy simulation (LES)-level resolution that converge rapidly to the direct numerical simulation (DNS) results. The combination of the level set method and RBVMS has been shown to be an effective method for accurate and robust simulation of free surface flows [56] and bubble dynamics [33]. This effectiveness is attributed to the flexibility of RBVMS with respect to different discretizations, such as FEM [56] or iso-geometric analysis (IGA) [56], as well as to the stability and consistency the method brings for a wide range of flow regimes, both laminar and turbulent.

Phase transition between solid and liquid is considered in this present work. Surface tension and Marangoni effects are included in the formulation, and are handled through the continuum surface force (CSF) model of Brackbill et al. [59]. To achieve better performance of multi-phase simulation, a re-distancing approach for the level set field [40,41,56] is used in this paper. The above-mentioned challenges result in many additional, non-smooth terms in the governing equations, such as surface tension terms in the momentum equations and a latent heat term in the energy conservation equation, and highly variable phase-dependent material properties. This makes the governing equations difficult to solve by traditional loosely coupled approaches, especially for realistic industrial applications. Several previous efforts indicated that to achieve robust and stable simulation for coupled problems involving high property ratios between different physical domains, such as fluid structure interaction for hydrofoils [60] and floating wind turbines [39], cardiovascular simulations [61], and free surface modeling for ship hydrodynamics [41], strong solution coupling strategies are required [62]. For gas–liquid–solid systems common in manufacturing processes, the density ratio between condensed and gas phases may be of order 10^4. In order to achieve better robustness and stability, we propose a fully coupled solution strategy using a Flexible GMRES solver. A fully coupled strategy requires the off-diagonal block entries in the Jacobian matrix in the coupled linear system. To avoid assembling these off-diagonal block entries, which may not only be complex to derive and compute but may also increase the condition number of the Jacobian matrix because of the different scales between different variables of this multi-physics problem, we implement a matrix-free technique using a Flexible GMRES solver. Such a combination produces an effective solution strategy for the thermal multi-phase flows with great robustness, accuracy and efficiency. To the best knowledge of the authors, this is the first FEM-based computational thermal multi-phase formulation that captures the dynamics of both gas phase and condensed phases, interface deformation, surface tension, and phase transition simultaneously.

The paper is outlined as follows. The governing equations, including the level set method, the Navier–Stokes equations and the energy conservation equation are presented in Section 2. Section 3 presents the full semi-discrete formulation of thermal multi-phase flows. Re-distancing and density-scaled continuum surface force model are also presented in this section. The time integration algorithm is presented in Section 4. The fully coupled approach using Flexible GMRES solver is introduced in Section 5. In Section 6, we present four computations using the framework developed. Conclusions are drawn in Section 7.

2. Governing equations of thermal multi-phase fluid flow for gas–liquid–solid systems at the continuous level

The computational formulation in the present work is based on a unified model for thermal fluid flows that is similar to models widely used in the manufacturing community for welding and casting analysis [4,5,42–48]. In this model, the entire gas–liquid–solid system is governed by a single set of fluid mechanics equations with different material properties for different phases, where the solid is approximated as a fluid with very high viscosity to constrain non-rigid body deformation to be negligible. Surface tension (capillary force), Marangoni effect (thermo-capillary force), solid/liquid transition, and buoyancy force, are included in the governing equations. In the present work, solid stress

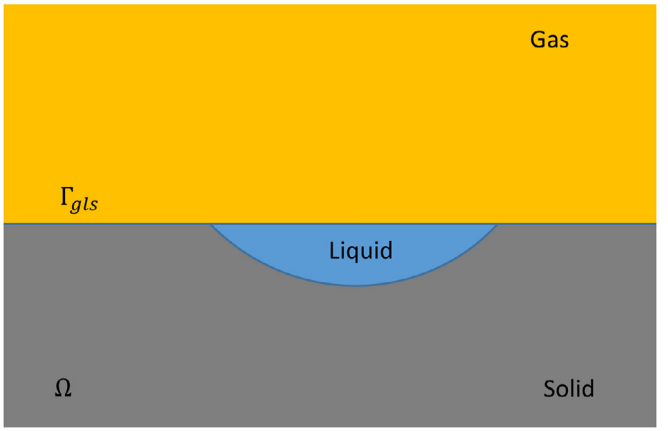

Fig. 2. A gas–liquid–solid system.

and recoil pressure of evaporation are not considered, and the same density is used for the solid and liquid phases, so that no volume change is caused by melting or solidification. With these assumptions, the governing equations of the thermal multi-phase fluid flow for gas–liquid–solid systems are presented as follows.

2.1. Level set method

Let Ω denote the spatial domain occupied by a gas–liquid–solid system, depicted in Fig. 2. The interface between the gas phase and liquid/solid phase is denoted by Γ_{gls}. In the level set method, the interface Γ_{gls} is represented implicitly by introducing a scalar level set field $\phi(\boldsymbol{x}, t)$ and setting

$$\Gamma_{gls} = \{\boldsymbol{x} \in \Omega \mid \phi(\boldsymbol{x}, t) = 0\}. \tag{1}$$

That is, the gas phase and liquid/solid phase are separated by the zero level set of ϕ. In the gas phase, ϕ takes negative value, while in the solid and liquid phase, ϕ takes positive value. The level set field moves with the material, thus the evolution of the level set field is governed by the following convection equation

$$\frac{\partial \phi}{\partial t} + \boldsymbol{u} \cdot \nabla \phi = 0, \tag{2}$$

where $\boldsymbol{u}$ is the flow velocity.

A given material property χ (such as density, viscosity, specific heat capacity, and heat conductivity, etc.) at each point of the domain is computed using the following formula:

$$\chi(\phi, f_L) = \chi_g[1 - H(\phi)] + [f_L \chi_l + (1 - f_L)\chi_s]\, H(\phi), \tag{3}$$

where χ_g, χ_l and χ_s are the corresponding specific material property for gas, liquid and solid phase, respectively, f_L is the liquid fraction, the model for which will be described below, and $H(\phi)$ is the Heaviside function, defined as

$$H(\phi) = \begin{cases} 0 & \text{if } \phi < 0 \\ 1/2 & \text{if } \phi = 0 \\ 1 & \text{if } \phi > 0. \end{cases} \tag{4}$$

2.2. Navier–Stokes equations

Since densities of the liquid and solid phases are equal in the present work, density is a function only of the level set field. Furthermore, by Eq. (2), the material derivative of the density is zero, and the incompressible form of the

Navier–Stokes equation describes the combined system:

$$\rho(\phi)\left(\frac{\partial \boldsymbol{u}}{\partial t}+\boldsymbol{u}\cdot\nabla\boldsymbol{u}\right)-\nabla\cdot\boldsymbol{\sigma}-\rho\boldsymbol{g}-\boldsymbol{f}_{gls}=\boldsymbol{0} \tag{5}$$

$$\nabla\cdot\boldsymbol{u}=0, \tag{6}$$

where $\boldsymbol{u}$ is the fluid velocity, ρ is the density, $\boldsymbol{g}$ is the gravitational acceleration vector, and $\boldsymbol{\sigma}(\mathbf{u}, p)$ is the Cauchy stress, defined as

$$\boldsymbol{\sigma}(\mathbf{u}, p)=-p\boldsymbol{I}+2\mu(\phi, f_L)\nabla^s\boldsymbol{u}, \tag{7}$$

where p is the pressure, μ is the dynamic viscosity, and $\boldsymbol{I}$ is the identity matrix, ∇^s is the symmetric gradient operator. Finally, $\boldsymbol{f}_{gls}$ is the interfacial force on the gas–liquid interface, which will be defined later.

To inhibit fluid motion in the solid phase, there are two popular approaches widely used in manufacturing simulations. The first option is to use a very large viscosity for the solid phase [4,5]. The second is to add another Darcy force term $-D_c\boldsymbol{u}$, based on the Carman–Kozeny model [63] to the left hand side of the momentum equation, where D_c is a large drag coefficient (some applications using this model can be found in [47,48]). In the present work, the first approach is employed.

2.3. Energy equation

The conservation equation of the enthalpy $\rho(c_pT+f_LL)$, incorporating fluid flow and heat conduction, is given as

$$\rho(\phi)c_p(\phi, f_L)\left(\frac{\partial T}{\partial t}+\boldsymbol{u}\cdot\nabla T\right)+\rho(\phi)L\left(\frac{\partial f_L}{\partial t}+\boldsymbol{u}\cdot\nabla f_L\right)-\nabla\cdot(\kappa(\phi, f_L)\nabla T)-Q_T=0, \tag{8}$$

where T is the temperature, C_p is the specific heat capacity, L is the latent heat during phase change, κ is the thermal conductivity and Q_T is an energy source term. In this paper, we assume that the liquid fraction follows a linear profile in the melting interval [64], thus the functional form of f_L is

$$f_L=\begin{cases}0 & \text{if } T\leqslant T_s\\ \dfrac{T-T_s}{T_l-T_s} & \text{if } T_s<T<T_l\\ 1 & \text{if } T\geqslant T_l\end{cases} \tag{9}$$

where T_s and T_l are the solidus and liquidus temperatures, respectively.

The above equations, together with suitably chosen initial and boundary conditions, constitute the thermal multi-phase flow formulation for gas–liquid–solid systems at the continuous level.

3. Numerical formulation

3.1. RBVMS

To numerically solve the coupled Navier–Stokes, level set and energy conservation equations, a residual-based variational multi-scale formulation (RBVMS) is employed. RBVMS relies on a scale decomposition of the physical variables (velocity, pressure, level set and temperature fields) combined with variational projections. This decomposition involving the large scales (those explicitly captured by the mesh) and the fine scales (subgrid scales, which need to be modeled) can be written

$$\boldsymbol{u}=\boldsymbol{u}^h+\boldsymbol{u}' \tag{10}$$

$$p=p^h+p' \tag{11}$$

$$\phi=\phi^h+\boldsymbol{\phi}' \tag{12}$$

$$T=T^h+T'. \tag{13}$$

Let $\mathcal{V}^h$ denote the set of discrete trial functions for the velocity, pressure, level set and temperature unknowns $\{\boldsymbol{u}^h, p^h, \phi^h, T^h\}$, and let $\mathcal{W}^h$ denote the set of discrete test functions for the linear-momentum, continuity, level set and

energy conservation equations $\{\mathbf{w}^h, q^h, \eta^h, \psi^h\}$. The formulation for thermal multi-phase flows is stated as follows: Find $\{\boldsymbol{u}^h, p^h, \phi^h, T^h\} \in \mathcal{V}^h$, such that $\forall\{\mathbf{w}^h, q^h, \eta^h, \psi^h\} \in \mathcal{W}^h$,

$$
\begin{aligned}
&\int_\Omega \boldsymbol{w}^h \cdot \rho\left(\frac{\partial \boldsymbol{u}^h}{\partial t} + \boldsymbol{u}^h \cdot \nabla \boldsymbol{u}^h - \boldsymbol{g}\right) \mathrm{d}\Omega - \int_\Omega \boldsymbol{w}^h \cdot \boldsymbol{f}_{gls}\, \mathrm{d}\Omega \\
&+ \int_\Omega \nabla \boldsymbol{w}^h : \boldsymbol{\sigma}(\boldsymbol{u}^h, p^h)\, \mathrm{d}\Omega - \int_{\Gamma_h} \boldsymbol{w}^h \cdot \mathbf{h}\, \mathrm{d}\Gamma + \int_\Omega q^h \nabla \cdot \boldsymbol{u}^h\, \mathrm{d}\Omega \\
&+ \int_\Omega \eta^h \left(\frac{\partial \phi^h}{\partial t} + \boldsymbol{u}^h \cdot \nabla \phi^h\right) \mathrm{d}\Omega \\
&+ \int_\Omega \psi^h \rho C_p \left(\frac{\partial T^h}{\partial t} + \boldsymbol{u}^h \cdot \nabla T^h\right) \mathrm{d}\Omega + \int_\Omega \psi^h \rho L \left(\frac{\partial f_L^h}{\partial t} + \boldsymbol{u}^h \cdot \nabla f_L^h\right) \mathrm{d}\Omega \\
&+ \int_\Omega \nabla \psi^h \kappa \cdot \nabla T^h\, \mathrm{d}\Omega - \int_\Omega \psi^h Q_T\, \mathrm{d}\Omega - \int_{\Gamma_{ht}} \psi^h h_T\, \mathrm{d}\Gamma \\
&- \sum_{e=1}^{nel} \int_{\Omega^e} \left(\rho \boldsymbol{u}^h \cdot \nabla \boldsymbol{w}^h + \nabla q^h\right) \cdot \boldsymbol{u}'(\boldsymbol{u}^h, p^h)\, \mathrm{d}\Omega \\
&- \sum_{e=1}^{nel} \int_{\Omega^e} \nabla \cdot \boldsymbol{w}^h p'(\boldsymbol{u}^h)\, \mathrm{d}\Omega + \sum_{e=1}^{nel} \int_{\Omega^e} \rho \boldsymbol{w}^h \cdot [\boldsymbol{u}'(\boldsymbol{u}^h, p^h) \cdot \nabla \boldsymbol{u}^h]\, \mathrm{d}\Omega \\
&- \sum_{e=1}^{nel} \int_{\Omega^e} \rho \nabla \boldsymbol{w}^h : [\boldsymbol{u}'(\boldsymbol{u}^h, p^h)] \otimes [\boldsymbol{u}'(\boldsymbol{u}^h, p^h)]\, \mathrm{d}\Omega \\
&- \sum_{e=1}^{nel} \int_{\Omega^e} \boldsymbol{u}^h \cdot \nabla \eta^h \phi'(\boldsymbol{u}^h, \phi^h)\, \mathrm{d}\Omega \\
&- \sum_{e=1}^{nel} \int_{\Omega^e} \rho C_p \boldsymbol{u}^h \cdot \nabla \psi^h T'(\boldsymbol{u}^h, T^h)\, \mathrm{d}\Omega = 0.
\end{aligned} \tag{14}
$$

In the above equation, the first five lines correspond to the standard Galerkin formulation of Navier–Stokes, level set and energy conservation equations, while the rest correspond to the fine scale terms in the multi-scale expansion. In the fine scale terms, nel denotes the number elements, $\boldsymbol{h}$ denotes the applied traction, h_T denotes the applied heat flux, and $\boldsymbol{u}'(\boldsymbol{u}^h, p^h)$, $p'(\boldsymbol{u}^h)$, $\phi'(\phi^h, \boldsymbol{u}^h)$ and $T'(\phi^h, T^h)$ are fine scales of fluid velocity, pressure, level set and temperature fields. Similar to the RBVMS in [49], the fine scales are modeled to be proportional to the residuals of the strong form equations, given by

$$
\boldsymbol{u}'(\boldsymbol{u}^h, p^h) = -\frac{\tau_M}{\rho}\left(\rho \frac{\partial \boldsymbol{u}^h}{\partial t} + \rho \boldsymbol{u}^h \cdot \nabla \boldsymbol{u}^h - \nabla \cdot \boldsymbol{\sigma}(\boldsymbol{u}^h, p^h) - \rho \boldsymbol{g} - \boldsymbol{f}_{gls}\right) \tag{15}
$$

$$
p'(\boldsymbol{u}^h) = -\tau_C \rho \nabla \cdot \boldsymbol{u}^h \tag{16}
$$

$$
\phi'(\phi^h, \boldsymbol{u}^h) = -\tau_\phi \left(\frac{\partial \phi^h}{\partial t} + \boldsymbol{u}^h \cdot \nabla \phi^h\right) \tag{17}
$$

$$
T'(\phi^h, T^h) = -\frac{\tau_T}{\rho c_p}\left[\rho c_p \left(\frac{\partial T^h}{\partial t} + \boldsymbol{u}^h \cdot \nabla T^h\right) + \rho L \left(\frac{\partial f_L^h}{\partial t} + \boldsymbol{u}^h \cdot \nabla f_L^h\right) - \nabla \cdot (\kappa \nabla T^h) - Q_T\right], \tag{18}
$$

where τ_M, τ_C, τ_ϕ and τ_T are the stabilization parameters [65–71]. In the present work, these parameters are chosen as

$$
\tau_M = \left(\frac{4}{\Delta t^2} + \boldsymbol{u}^h \cdot \mathbf{G} \boldsymbol{u}^h + C_I \left(\frac{\mu}{\rho}\right)^2 \mathbf{G} : \mathbf{G}\right)^{-1/2}, \tag{19}
$$

$$
\tau_C = \frac{1}{tr(\mathbf{G})\tau_M}, \tag{20}
$$

$$\tau_\phi = \left(\frac{4}{\Delta t^2} + \boldsymbol{u}^h \cdot \mathbf{G}\boldsymbol{u}^h \right)^{-1/2}, \tag{21}$$

$$\tau_T = \left(\frac{4}{\Delta t^2} + \boldsymbol{u}^h \cdot \mathbf{G}\boldsymbol{u}^h + C_I \left(\frac{\kappa}{\rho c_p} \right)^2 \mathbf{G} : \mathbf{G} \right)^{-1/2}, \tag{22}$$

where C_I is a dimensionless positive constant derived from an element-wise inverse estimate [72], $\mathbf{G}$ is the element metric tensor defined by $\mathbf{G} = \left(\frac{\partial \boldsymbol{\xi}}{\partial \mathbf{x}} \right)^T \frac{\partial \boldsymbol{\xi}}{\partial \mathbf{x}}$, and $\frac{\partial \boldsymbol{\xi}}{\partial \mathbf{x}}$ is the inverse of the Jacobian of the transformation between the physical element and its parametric counterpart [33]. Note that the above residuals and stabilization parameters of Eq. (15) through Eq. (22) are evaluated at the quadrature points. The second derivatives of coarse scale variables that appear in (15) and (18) can be evaluated directly for higher-order shape functions, such as those used in IGA as in our previous work for bubble dynamics [33]. For tri-linear finite element shape functions, second derivatives may be obtained from a L_2 projection, or may be assumed small on element interiors and neglected. The latter approach is used in the current work.

For a detailed presentation of the RBVMS methodology, readers are referred to the original development in [49], and its applications to single-phase turbulent flows [50,51], free-surface flows [38,39] and stratified flows [56]. It should be noted that while RBVMS was originally developed for large eddy simulations (LES) of turbulent flows, it is also an accurate and robust methodology for stabilized simulations of laminar incompressible flows. In this setting, RBVMS provides a unified stabilization approach in lieu of the combination of upwinding and pressure stabilization strategies that would otherwise be required for a finite element discretization of the coupled equations.

3.2. Re-distancing the level set field

At the discrete level, in place of its sharp counterpart given by Eq. (4), a regularized version of the Heaviside function H_ϵ is employed:

$$H_\epsilon(\phi) = \begin{cases} 0 & \text{if } \phi < -\epsilon \\ \frac{1}{2}\left(1 + \frac{\phi}{\epsilon} + \frac{1}{\pi}\sin\left(\frac{\phi\pi}{\epsilon}\right)\right) & \text{if } |\phi| \le \epsilon \\ 1 & \text{if } \phi > \epsilon, \end{cases} \tag{23}$$

where $\epsilon \sim O(h)$ defines the local width of the interface between the gas phase and liquid/solid phase. As the mesh is refined, $\epsilon \to 0$.

Regularization of the Heaviside function used in Eq. (3) puts a requirement on the level set function to satisfy a so-called signed-distance property. To enforce this requirement, we "re-distance" ϕ after every physical time step by replacing it with ϕ_d, where the latter satisfies the Eikonal equation,

$$\left|\nabla \phi_d\right| = 1 \text{ in } \Omega, \tag{24}$$

and the interior constraint,

$$\phi_d = \phi = 0 \text{ on } \Gamma_t, \tag{25}$$

which gives the correct position of the interface between the gas phase and liquid/solid phase at all times.

Following the work in [30,38–41,73,74], we introduce a "pseudo-time" variable $\tilde{t}$ and re-state the above problem as: Given ϕ from Eq. (2), find ϕ_d that satisfies

$$\begin{aligned} &\frac{\partial \phi_d}{\partial \tilde{t}} + \text{sgn}(\phi)(\left|\nabla \phi_d\right| - 1) = 0 \text{ in } \Omega, \\ &\phi_d = \phi = 0 \text{ on } \Gamma_t, \\ &\phi_d(\boldsymbol{x}, 0) = \phi(\boldsymbol{x}), \end{aligned} \tag{26}$$

where $\text{sgn}(\phi)$ is the sign function.

In order to satisfy the above equations, the following weak formulation at the discrete level is adopted: Given ϕ^h_{n+1} (level set function at the end of the time step), find ϕ^h_d, such that $\forall \eta^h_d$,

$$\begin{aligned}
&\int_\Omega \eta^h_d \left(\frac{\partial \phi^h_d}{\partial \tilde{t}} + \mathbf{a}\cdot\nabla\phi^h_d - S_\epsilon(\phi^h_{n+1}) \right) \mathrm{d}\Omega \\
&+ \int_\Omega \tau_{\phi_d} \mathbf{a}\cdot\nabla\eta^h_d \left(\frac{\partial \phi^h_d}{\partial \tilde{t}} + \mathbf{a}\cdot\nabla\phi^h_d - S_\epsilon(\phi^h_{n+1}) \right) \mathrm{d}\Omega \\
&+ \int_\Omega \eta^h_d \lambda_{pen} \frac{dH_\epsilon(\phi^h)}{d\phi^h} (\phi^h_d - \phi^h_{n+1}) \,\mathrm{d}\Omega = 0,
\end{aligned} \tag{27}$$

where $S_\epsilon(\phi) = 2H_\epsilon(\phi) - 1$ is the regularized sign function, $\mathbf{a} = S_\epsilon(\phi^h_{n+1})\nabla\phi^h_d \Big/ \left|\nabla\phi^h_d\right|$ is the effective "convective" velocity, λ_{pen} is a penalty parameter, and τ_{ϕ_d} is the stabilization parameter given by

$$\tau_{\phi_d} = \left(\frac{4}{\Delta\tilde{t}^2} + \mathbf{a}\cdot\mathbf{G}\mathbf{a} \right)^{-1/2}. \tag{28}$$

The formulation given by Eq. (27) is essentially a stabilized method for the pseudo-time-dependent Eikonal equation, with additional penalty terms employed to satisfy the interior constraint given by Eq. (25).

The Backward Euler method is employed to integrate Eq. (27) in pseudo-time at each physical time step, with ϕ^h_d set to ϕ^h_{n+1} at $\tilde{t} = 0$. Only a few pseudo-time steps are taken for efficiency, and a new level set field ϕ^h_d is generated with the zero level set coincident with that of ϕ^h. The size of the pseudo-time step is chosen based on the convective CFL condition for the Eikonal equation, and is computed as

$$\Delta\tilde{t} = 2\gamma \min_{\mathbf{x}\in\Omega_t} (\mathbf{a}\cdot\mathbf{G}\mathbf{a})^{-1/2}, \tag{29}$$

where γ is the Courant number taken to be $O(1)$.

Re-distancing of the level set field may violate mass balance. To correct this, the global mass restoration method, which is proposed in [75], can be used, provided that the same density are used for both liquid and solid phase. For more details of the approach, readers are referred to [75] as well as additional Refs. [33,38].

3.3. Interfacial forces

The continuum surface force (CSF) model [59] is used to incorporate interfacial forces into the thermal multi-phase flow formulation. For this, $\boldsymbol{f}_{gls}$ in Eq. (5) is given by

$$\boldsymbol{f}_{gls} = \left\{ \sigma_s \kappa_s \boldsymbol{n} + \frac{d\sigma_s}{dT} \left[\nabla T - (\nabla T \cdot \boldsymbol{n})\boldsymbol{n} \right] \right\} \delta, \tag{30}$$

where the surface tension coefficient is denoted by σ_s, $\frac{d\sigma_s}{dT}$ is the Marangoni coefficient, and $\boldsymbol{n}$ is the unit normal vector to the interface given by

$$\boldsymbol{n} = -\frac{\nabla\phi}{\left|\nabla\phi\right|}. \tag{31}$$

In addition, in Eq. (30), κ_s is the mean curvature, which can be computed from the level set field as

$$\kappa_s = -\nabla\cdot\boldsymbol{n} = -\frac{\left|\nabla\phi\right|^2 tr(\boldsymbol{\psi}(\phi)) - \nabla\phi^T \boldsymbol{\psi}(\phi)\nabla\phi}{\left|\nabla\phi\right|^3}, \tag{32}$$

where $\boldsymbol{\psi}(\phi)$ is the matrix of second derivatives, or the Hessian, of ϕ, which is calculated by a L_2 projection in the present work using linear FEM. Please note the current formulation can be incorporated with other types of discretization, such as higher order Isogeometric Analysis (IGA) [76,77] in which Eq. (32) can be directly applied. For the isothermal multi-phase flow simulations with surface tension using IGA and its applications to bubble rising dynamics, readers are referred to [33].

Unlike our previous work [33], in the present work, the density-scaled CSF model, which was used in the original CSF model paper [59] and has been proved to perform better for the cases with high density ratio in [78], is adopted

and defined as

$$\delta = \frac{2\rho(\phi, f_L)\delta_\epsilon(\phi)}{\rho_g + \rho_l}, \tag{33}$$

where δ_ϵ is the regularized Dirac delta function, defined as

$$\delta_\epsilon(\phi) = \frac{dH_\epsilon(\phi)}{d\phi}. \tag{34}$$

4. Time integration

The generalized-α method [79] is adopted for time integration and presented as follows. Let $\boldsymbol{U}, \dot{\boldsymbol{U}}$ and $\boldsymbol{P}$ denote the vectors of nodal degrees-of-freedom of fluid velocity, its time derivative, and pressure, respectively. Let $\boldsymbol{\Phi}$ and $\dot{\boldsymbol{\Phi}}$ denote the vectors of nodal degrees-of-freedom of the level set function and its time derivative. Let $\boldsymbol{\Theta}$ and $\dot{\boldsymbol{\Theta}}$ denote the vectors of nodal degrees-of-freedom of the temperature and its time derivative.

Application of the generalized-α method to the coupled thermal fluid flow formulation leads to a coupled, nonlinear equation systems that need to be solved at every time step, namely: find $\boldsymbol{U}_{n+1}, \dot{\boldsymbol{U}}_{n+1}, \boldsymbol{P}_{n+1}, \boldsymbol{\Phi}_{n+1}, \dot{\boldsymbol{\Phi}}_{n+1}, \boldsymbol{\Theta}_{n+1}$ and $\dot{\boldsymbol{\Theta}}_{n+1}$, such that,

$$\begin{cases} \boldsymbol{N}_M(\boldsymbol{U}_{n+\alpha_f}, \dot{\boldsymbol{U}}_{n+\alpha_m}, \boldsymbol{P}_{n+1}, \boldsymbol{\Phi}_{n+\alpha_f}, \dot{\boldsymbol{\Phi}}_{n+\alpha_m}, \boldsymbol{\Theta}_{n+\alpha_f}, \dot{\boldsymbol{\Theta}}_{n+\alpha_m}) = \boldsymbol{0} \\ \boldsymbol{N}_C(\boldsymbol{U}_{n+\alpha_f}, \dot{\boldsymbol{U}}_{n+\alpha_m}, \boldsymbol{P}_{n+1}, \boldsymbol{\Phi}_{n+\alpha_f}, \dot{\boldsymbol{\Phi}}_{n+\alpha_m}, \boldsymbol{\Theta}_{n+\alpha_f}, \dot{\boldsymbol{\Theta}}_{n+\alpha_m}) = \boldsymbol{0} \\ \boldsymbol{N}_L(\boldsymbol{U}_{n+\alpha_f}, \dot{\boldsymbol{U}}_{n+\alpha_m}, \boldsymbol{P}_{n+1}, \boldsymbol{\Phi}_{n+\alpha_f}, \dot{\boldsymbol{\Phi}}_{n+\alpha_m}, \boldsymbol{\Theta}_{n+\alpha_f}, \dot{\boldsymbol{\Theta}}_{n+\alpha_m}) = \boldsymbol{0} \\ \boldsymbol{N}_T(\boldsymbol{U}_{n+\alpha_f}, \dot{\boldsymbol{U}}_{n+\alpha_m}, \boldsymbol{P}_{n+1}, \boldsymbol{\Phi}_{n+\alpha_f}, \dot{\boldsymbol{\Phi}}_{n+\alpha_m}, \boldsymbol{\Theta}_{n+\alpha_f}, \dot{\boldsymbol{\Theta}}_{n+\alpha_m}) = \boldsymbol{0}, \end{cases} \tag{35}$$

where α_m, α_f and γ are the real-valued parameters of the generalized-α method and chosen based on the stability and accuracy [79]. $\boldsymbol{N}_M, \boldsymbol{N}_C, \boldsymbol{N}_L$ and $\boldsymbol{N}_T$ are the vectors of nodal residuals of fluid momentum, continuity, level set, and energy conservation equations, respectively, and the intermediate-level solutions are given by

$$\begin{aligned} \dot{\boldsymbol{U}}_{n+\alpha_m} &= \dot{\boldsymbol{U}}_n + \alpha_m(\dot{\boldsymbol{U}}_{n+1} - \dot{\boldsymbol{U}}_n) \\ \boldsymbol{U}_{n+\alpha_f} &= \boldsymbol{U}_n + \alpha_f(\boldsymbol{U}_{n+1} - \boldsymbol{U}_n) \\ \dot{\boldsymbol{\Phi}}_{n+\alpha_m} &= \dot{\boldsymbol{\Phi}}_n + \alpha_m(\dot{\boldsymbol{\Phi}}_{n+1} - \dot{\boldsymbol{\Phi}}_n) \\ \boldsymbol{\Phi}_{n+\alpha_f} &= \boldsymbol{\Phi}_n + \alpha_f(\boldsymbol{\Phi}_{n+1} - \boldsymbol{\Phi}_n) \\ \dot{\boldsymbol{\Theta}}_{n+\alpha_m} &= \dot{\boldsymbol{\Theta}}_n + \alpha_m(\dot{\boldsymbol{\Theta}}_{n+1} - \dot{\boldsymbol{\Theta}}_n) \\ \boldsymbol{\Theta}_{n+\alpha_f} &= \boldsymbol{\Theta}_n + \alpha_f(\boldsymbol{\Theta}_{n+1} - \boldsymbol{\Theta}_n). \end{aligned} \tag{36}$$

The quantities at time level t_n are assumed known. In addition to the above equations, the relationships between nodal degrees-of-freedom and their time derivatives are given by the following formulas:

$$\begin{aligned} \boldsymbol{U}_{n+1} &= \boldsymbol{U}_n + \Delta t\left[(1-\gamma)\dot{\boldsymbol{U}}_n + \gamma\dot{\boldsymbol{U}}_{n+1}\right] \\ \boldsymbol{\Phi}_{n+1} &= \boldsymbol{\Phi}_n + \Delta t\left[(1-\gamma)\dot{\boldsymbol{\Phi}}_n + \gamma\,\dot{\boldsymbol{\Phi}}_{n+1}\right] \\ \boldsymbol{\Theta}_{n+1} &= \boldsymbol{\Theta}_n + \Delta t\left[(1-\gamma)\dot{\boldsymbol{\Theta}}_n + \gamma\,\dot{\boldsymbol{\Theta}}_{n+1}\right] \end{aligned} \tag{37}$$

where γ is a real-valued parameter between 0 and 1. Newton's method is employed to solve the nonlinear equation system, which results in the following two-stage predictor–multicorrector algorithm.

Predictor stage. Initialize:

$$\begin{aligned} \dot{\boldsymbol{U}}^0_{n+1} &= \frac{\gamma-1}{\gamma}\dot{\boldsymbol{U}}_n \\ \boldsymbol{U}^0_{n+1} &= \boldsymbol{U}_n \\ \boldsymbol{P}^0_{n+1} &= \boldsymbol{P}_n \end{aligned}$$

$$\begin{aligned}
\dot{\boldsymbol{\Phi}}^0_{n+1} &= \frac{\gamma-1}{\gamma}\,\dot{\boldsymbol{\Phi}}_n \\
\boldsymbol{\Phi}^0_{n+1} &= \boldsymbol{\Phi}_n \\
\dot{\boldsymbol{\Theta}}^0_{n+1} &= \frac{\gamma-1}{\gamma}\,\dot{\boldsymbol{\Theta}}_n \\
\boldsymbol{\Theta}^0_{n+1} &= \boldsymbol{\Theta}_n
\end{aligned} \tag{38}$$

where superscript '0' is the initial value of the Newton-iteration counter.

Multicorrector stage. Repeat the following steps until convergence at the time level t_{n+1}:

1. Evaluate the iterates at the intermediate time level:

$$\begin{aligned}
\dot{\boldsymbol{U}}^l_{n+\alpha_m} &= \dot{\boldsymbol{U}}_n + \alpha_m(\dot{\boldsymbol{U}}^{l-1}_{n+1} - \dot{\boldsymbol{U}}_n) \\
\boldsymbol{U}^l_{n+\alpha_f} &= \boldsymbol{U}_n + \alpha_f(\boldsymbol{U}^{l-1}_{n+1} - \boldsymbol{U}_n) \\
\dot{\boldsymbol{\Phi}}^l_{n+\alpha_m} &= \dot{\boldsymbol{\Phi}}_n + \alpha_m(\dot{\boldsymbol{\Phi}}^{l-1}_{n+1} - \dot{\boldsymbol{\Phi}}_n) \\
\boldsymbol{\Phi}^l_{n+\alpha_f} &= \boldsymbol{\Phi}_n + \alpha_f(\boldsymbol{\Phi}^{l-1}_{n+1} - \boldsymbol{\Phi}_n) \\
\dot{\boldsymbol{\Theta}}^l_{n+\alpha_m} &= \dot{\boldsymbol{\Theta}}_n + \alpha_m(\dot{\boldsymbol{\Theta}}^{l-1}_{n+1} - \dot{\boldsymbol{\Theta}}_n) \\
\boldsymbol{\Theta}^l_{n+\alpha_f} &= \boldsymbol{\Theta}_n + \alpha_f(\boldsymbol{\Theta}^{l-1}_{n+1} - \boldsymbol{\Theta}_n)
\end{aligned} \tag{39}$$

where l is the Newton-iteration counter.

2. Use the intermediate values to assemble $\boldsymbol{N}^l_M$, $\boldsymbol{N}^l_C$, $\boldsymbol{N}^l_L$ and $\boldsymbol{N}^l_T$, the discrete residuals of the momentum, continuity, level set, energy conservation equations and the corresponding matrices of the linear equation system at lth iteration:

$$\begin{cases}
\dfrac{\partial \boldsymbol{N}_M}{\partial \dot{\boldsymbol{U}}_{n+1}}\bigg|_l \Delta\dot{\boldsymbol{U}}^l_{n+1} + \dfrac{\partial \boldsymbol{N}_M}{\partial \boldsymbol{P}_{n+1}}\bigg|_l \Delta\boldsymbol{P}^l_{n+1} + \dfrac{\partial \boldsymbol{N}_M}{\partial \dot{\boldsymbol{\Phi}}_{n+1}}\bigg|_l \Delta\dot{\boldsymbol{\Phi}}^l_{n+1} + \dfrac{\partial \boldsymbol{N}_M}{\partial \ddot{\boldsymbol{\Theta}}_{n+1}}\bigg|_l \Delta\dot{\boldsymbol{\Theta}}^l_{n+1} = -\boldsymbol{N}^l_M \\
\dfrac{\partial \boldsymbol{N}_C}{\partial \dot{\boldsymbol{U}}_{n+1}}\bigg|_l \Delta\dot{\boldsymbol{U}}^l_{n+1} + \dfrac{\partial \boldsymbol{N}_C}{\partial \boldsymbol{P}_{n+1}}\bigg|_l \Delta\boldsymbol{P}^l_{n+1} + \dfrac{\partial \boldsymbol{N}_C}{\partial \dot{\boldsymbol{\Phi}}_{n+1}}\bigg|_l \Delta\dot{\boldsymbol{\Phi}}^l_{n+1} + \dfrac{\partial \boldsymbol{N}_C}{\partial \ddot{\boldsymbol{\Theta}}_{n+1}}\bigg|_l \Delta\dot{\boldsymbol{\Theta}}^l_{n+1} = -\boldsymbol{N}^l_C \\
\dfrac{\partial \boldsymbol{N}_L}{\partial \dot{\boldsymbol{U}}_{n+1}}\bigg|_l \Delta\dot{\boldsymbol{U}}^l_{n+1} + \dfrac{\partial \boldsymbol{N}_L}{\partial \boldsymbol{P}_{n+1}}\bigg|_l \Delta\boldsymbol{P}^l_{n+1} + \dfrac{\partial \boldsymbol{N}_L}{\partial \dot{\boldsymbol{\Phi}}_{n+1}}\bigg|_l \Delta\dot{\boldsymbol{\Phi}}^l_{n+1} + \dfrac{\partial \boldsymbol{N}_L}{\partial \ddot{\boldsymbol{\Theta}}_{n+1}}\bigg|_l \Delta\dot{\boldsymbol{\Theta}}^l_{n+1} = -\boldsymbol{N}^l_L \\
\dfrac{\partial \boldsymbol{N}_T}{\partial \dot{\boldsymbol{U}}_{n+1}}\bigg|_l \Delta\dot{\boldsymbol{U}}^l_{n+1} + \dfrac{\partial \boldsymbol{N}_T}{\partial \boldsymbol{P}_{n+1}}\bigg|_l \Delta\boldsymbol{P}^l_{n+1} + \dfrac{\partial \boldsymbol{N}_T}{\partial \dot{\boldsymbol{\Phi}}_{n+1}}\bigg|_l \Delta\dot{\boldsymbol{\Phi}}^l_{n+1} + \dfrac{\partial \boldsymbol{N}_T}{\partial \ddot{\boldsymbol{\Theta}}_{n+1}}\bigg|_l \Delta\dot{\boldsymbol{\Theta}}^l_{n+1} = -\boldsymbol{N}^l_T.
\end{cases} \tag{40}$$

Note that the system is solved for time derivatives of velocity, pressure, time derivative of level set and time derivative of temperature.

3. Update the solutions as follows:

$$\begin{aligned}
\dot{\boldsymbol{U}}^l_{n+1} &= \dot{\boldsymbol{U}}^{l-1}_{n+1} + \Delta\dot{\boldsymbol{U}}^l_{n+1} \\
\boldsymbol{U}^l_{n+1} &= \boldsymbol{U}^{l-1}_{n+1} + \gamma\,\Delta t\,\Delta\dot{\boldsymbol{U}}^l_{n+1} \\
\boldsymbol{P}^l_{n+1} &= \boldsymbol{P}^{l-1}_{n+1} + \Delta\boldsymbol{P}^l_{n+1} \\
\dot{\boldsymbol{\Phi}}^l_{n+1} &= \dot{\boldsymbol{\Phi}}^{l-1}_{n+1} + \Delta\dot{\boldsymbol{\Phi}}^l_{n+1} \\
\boldsymbol{\Phi}^l_{n+1} &= \boldsymbol{\Phi}^{l-1}_{n+1} + \gamma\,\Delta t\,\dot{\boldsymbol{\Phi}}^l_{n+1} \\
\dot{\boldsymbol{\Theta}}^l_{n+1} &= \dot{\boldsymbol{\Theta}}^{l-1}_{n+1} + \Delta\dot{\boldsymbol{\Theta}}^l_{n+1} \\
\boldsymbol{\Theta}^l_{n+1} &= \boldsymbol{\Theta}^{l-1}_{n+1} + \gamma\,\Delta t\,\dot{\boldsymbol{\Theta}}^l_{n+1}
\end{aligned} \tag{41}$$

and increase the Newton-iteration counter by one. For the generalized α method, it has been shown that second-order accuracy in time is achieved provided that $\gamma = \frac{1}{2} + \alpha_m - \alpha_f$, while unconditionally stability is attained provided that $\alpha_m > \alpha_f \geq \frac{1}{2}$. See [62,80] for more details.

5. Fully coupled approach: flexible GMRES

For thermal multi-phase flows, many non-smooth terms appear in the governing equations, such as surface tension terms in the momentum equations and a latent heat term in the energy conservation equation. In addition, in a typical manufacturing process involving molten metal, the density ratio between the liquid/solid phase and the gas phase is $O(10^3)$–$O(10^4)$, making stable and robust thermal multi-phase simulations very challenging. In order to increase robustness, in this work the proposed formulation is solved in a fully coupled fashion. In particular, the large linear system given in Eq. (40) is solved at each Newton iteration as a monolithic matrix equation using the Generalized Minimal Residual (GMRES) iterative solver. However, forming the full analytical Jacobian matrix implied by Eq. (40), especially the off-diagonal blocks, is mathematically and computationally tedious; furthermore, the resulting matrix may be ill-conditioned due to different scales between different variables of this multi-physics problem. In order to avoid assembling the full Jacobian matrix while still treating the problem in a fully coupled way, a flexible-GMRES (FGMRES) technique with block preconditioning is adopted. This approach, which belongs to the class of matrix-free or Jacobian-free Newton–Krylov methods [81], was used by Johan et al. [82,83] for single phase flow simulations and later extended to fluid–structure interaction and free-surface flow simulations [39,60,84–86].

The matrix problem to be solved, Eq. (40), has the form

$$\boldsymbol{J}\Delta\boldsymbol{x}^{l+1} = -\boldsymbol{N}(\boldsymbol{x}^{l}) \tag{42}$$

where $\boldsymbol{J} = \partial\boldsymbol{N}/\partial\boldsymbol{x}$ is the Jacobian matrix, $\boldsymbol{x}^l$ is the vector of unknowns at Newton iteration l, $\Delta\boldsymbol{x}^{l+1}$ is the increment to be solved, and $\boldsymbol{N}(\boldsymbol{x}^l)$ is the residual computed at the current iteration. The preconditioned GMRES algorithm for solution of this matrix problem is an iterative scheme characterized by two operations that contribute the majority of the computational work: (1) multiplication of given vectors $\boldsymbol{v}$ by the left-hand side matrix (in this case $\boldsymbol{J}$), and (2) repeated solution of the related matrix problem $\boldsymbol{M}_{pre}\boldsymbol{w} = \boldsymbol{b}$, where the preconditioning matrix $\boldsymbol{M}_{pre}$ approximates $\boldsymbol{J}$ but leads to a matrix equation that can be solved more efficiently than the original equation. Both the matrix multiplication and preconditioner solve operations are required once at every iteration of the GMRES algorithm. Full details of the preconditioned GMRES algorithm can be found in [84]; here we describe the computation of these two main operations in the flexible GMRES approach.

5.1. Matrix-free Jacobian multiplication

Multiplication of a vector $\boldsymbol{v}$ by the Jacobian matrix $\boldsymbol{J}(\boldsymbol{x})$ can be approximated by a one-sided finite difference:

$$\boldsymbol{J}(\boldsymbol{x})\boldsymbol{v} = \frac{\partial\boldsymbol{N}(\boldsymbol{x})}{\partial\boldsymbol{x}}\boldsymbol{v} \approx \frac{1}{\varepsilon}\left(\boldsymbol{N}(\boldsymbol{x}+\varepsilon\boldsymbol{v}) - \boldsymbol{N}(\boldsymbol{x})\right) \tag{43}$$

where ε is a small scalar parameter. This approximation follows naturally from a first-order Taylor expansion of $\boldsymbol{N}(\boldsymbol{x}+\varepsilon\boldsymbol{v})$ about $\boldsymbol{x}$. In the case of the solution to Eq. (40), in which the matrix of interest is the Jacobian of the residual for the fully coupled system, this can be written:

$$\boldsymbol{J}\boldsymbol{v} \approx \frac{1}{\varepsilon}\begin{bmatrix} \boldsymbol{N}_M(\dot{\boldsymbol{U}}^l_{n+1}+\varepsilon\boldsymbol{v}_u, \boldsymbol{P}^l_{n+1}+\varepsilon\boldsymbol{v}_p, \dot{\boldsymbol{\Phi}}^l_{n+1}+\varepsilon\boldsymbol{v}_\phi, \dot{\boldsymbol{\Theta}}^l_{n+1}+\varepsilon\boldsymbol{v}_T) - \boldsymbol{N}_M(\dot{\boldsymbol{U}}^l_{n+1}, \boldsymbol{P}^l_{n+1}, \dot{\boldsymbol{\Phi}}^l_{n+1}, \dot{\boldsymbol{\Theta}}^l_{n+1}) \\ \boldsymbol{N}_C(\dot{\boldsymbol{U}}^l_{n+1}+\varepsilon\boldsymbol{v}_u, \boldsymbol{P}^l_{n+1}+\varepsilon\boldsymbol{v}_p, \dot{\boldsymbol{\Phi}}^l_{n+1}+\varepsilon\boldsymbol{v}_\phi, \dot{\boldsymbol{\Theta}}^l_{n+1}+\varepsilon\boldsymbol{v}_T) - \boldsymbol{N}_C(\dot{\boldsymbol{U}}^l_{n+1}, \boldsymbol{P}^l_{n+1}, \dot{\boldsymbol{\Phi}}^l_{n+1}, \dot{\boldsymbol{\Theta}}^l_{n+1}) \\ \boldsymbol{N}_L(\dot{\boldsymbol{U}}^l_{n+1}+\varepsilon\boldsymbol{v}_u, \boldsymbol{P}^l_{n+1}+\varepsilon\boldsymbol{v}_p, \dot{\boldsymbol{\Phi}}^l_{n+1}+\varepsilon\boldsymbol{v}_\phi, \dot{\boldsymbol{\Theta}}^l_{n+1}+\varepsilon\boldsymbol{v}_T) - \boldsymbol{N}_L(\dot{\boldsymbol{U}}^l_{n+1}, \boldsymbol{P}^l_{n+1}, \dot{\boldsymbol{\Phi}}^l_{n+1}, \dot{\boldsymbol{\Theta}}^l_{n+1}) \\ \boldsymbol{N}_T(\dot{\boldsymbol{U}}^l_{n+1}+\varepsilon\boldsymbol{v}_u, \boldsymbol{P}^l_{n+1}+\varepsilon\boldsymbol{v}_p, \dot{\boldsymbol{\Phi}}^l_{n+1}+\varepsilon\boldsymbol{v}_\phi, \dot{\boldsymbol{\Theta}}^l_{n+1}+\varepsilon\boldsymbol{v}_T) - \boldsymbol{N}_T(\dot{\boldsymbol{U}}^l_{n+1}, \boldsymbol{P}^l_{n+1}, \dot{\boldsymbol{\Phi}}^l_{n+1}, \dot{\boldsymbol{\Theta}}^l_{n+1}) \end{bmatrix}, \tag{44}$$

where $\boldsymbol{v}_u$, $\boldsymbol{v}_p$, $\boldsymbol{v}_\phi$, and $\boldsymbol{v}_T$ are the partitions of $\boldsymbol{v}$ corresponding respectively to the velocity, pressure, level set, and temperature degrees of freedom. The parameter ε must be small enough to lead to a good approximation of the Jacobian multiplication, but large enough to prevent machine round-off error from affecting the perturbation. In the present work, a value of (10^{-3}) is used and is found to give good results. More detailed approaches for choosing ε can be found in [81].

5.2. Preconditioning

The convergence speed of GMRES depends strongly on how well the preconditioning matrix $\boldsymbol{M}_{pre}$ approximates the full system matrix; a good preconditioner can greatly reduce the number of iterations, and therefore the number of

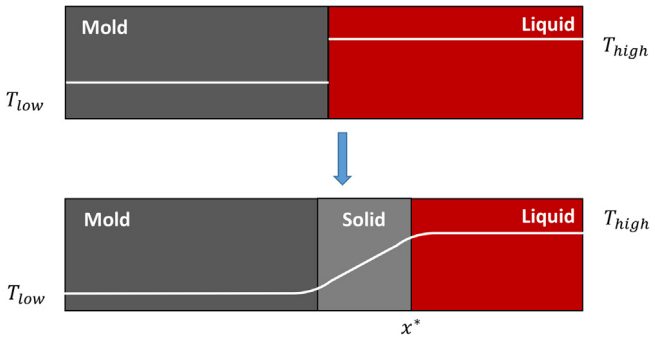

Fig. 3. A schematic drawing of the solidification of aluminum in a mold. Upper: initial temperature profile. Lower: temperature profile after solidification.

costly evaluations of the residual vector $\boldsymbol{N}$. In the FGMRES method, the preconditioning matrix is a block-diagonal approximation to the full Jacobian matrix, i.e.:

$$\boldsymbol{M}_{pre} = \begin{Bmatrix} \dfrac{\partial \boldsymbol{N}_M}{\partial \dot{\boldsymbol{U}}_{n+1}} & \dfrac{\partial \boldsymbol{N}_M}{\partial \boldsymbol{P}_{n+1}} & 0 & 0 \\ \dfrac{\partial \boldsymbol{N}_C}{\partial \dot{\boldsymbol{U}}_{n+1}} & \dfrac{\partial \boldsymbol{N}_C}{\partial \boldsymbol{P}_{n+1}} & 0 & 0 \\ 0 & 0 & \dfrac{\partial \boldsymbol{N}_L}{\partial \dot{\boldsymbol{\Phi}}_{n+1}} & 0 \\ 0 & 0 & 0 & \dfrac{\partial \boldsymbol{N}_T}{\partial \dot{\boldsymbol{\Theta}}_{n+1}} \end{Bmatrix}. \tag{45}$$

The implication of this form is that, in order to solve the preconditioner matrix system, $\boldsymbol{M}_{pre}\boldsymbol{w} = \boldsymbol{b}$, we solve individually for the *uncoupled* velocity–pressure, level set, and energy problems. Note that in this approach, the non-zero blocks of the matrix (such as $\partial \boldsymbol{N}_M / \partial \dot{\boldsymbol{U}}_{n+1}$) are fully formed and stored (that is, a matrix-free approach is not used for the preconditioner solve). The individual uncoupled systems can then be solved using a standard GMRES algorithm.

In summary, the FGMRES method combines an outer, matrix-free GMRES iteration loop over the fully coupled system with an inner preconditioner solution of the individual, block uncoupled systems of equations. With this approach, only a small number of outer iterations are required for accurate solution. For example, in the numerical examples shown in Sections 6.3 and 6.4, the relative tolerance for nonlinear and linear solves is set to 0.001. The maximum number of matrix-free outer iterations used is 4, while the numbers of GMRES iterations used at each preconditioning solution are 80, 30, and 40 for the Navier–Stokes, level set, and energy equations, respectively.

6. Numerical examples

6.1. Solidification of aluminum in a graphite mold

Solution of the energy equation with phase change is tested in this section. Consider the one-dimensional solidification process of a pure aluminum in a graphite mold, as depicted in Fig. 3. Pure liquid aluminum, initially with uniform temperature T_{high} greater than the melting temperature T_{melt}, occupies half of the domain $0\text{ m} < x \leq 0.4\text{ m}$. A graphite mold, initially with uniform temperature $T_{low} < T_{melt}$, occupies the other half domain of $-0.4\text{ m} \leq x \leq 0\text{ m}$. Solidification begins at time $t = 0$ by transferring heat into the mold. After some time, the temperature distributions in the mold, solid and liquid will correspond to the schematic depicted in Fig. 3 (lower). This problem provides valuable insight into the behavior of solidifying systems and the roles of various parameters.

The material properties of the graphite mold and aluminum are given in Table 1. A similar problem was investigated analytically in [87]. Unlike [87], the same density and heat capacity are used for the solid and liquid phases in order to be consistent with the zero convection assumption. The initial temperature of the liquid is $T_{high} = 973.15\text{ K}$, the mold has an initial temperature of $T_{low} = 298.15\text{ K}$, and the melting point for aluminum is $T_{melt} = 933.15\text{ K}$.

Table 1
Definition of material properties.

Materials	Graphite	Aluminum (solid)	Aluminum (liquid)
Density (kg/m^3)	2200	2555	2555
Specific heat (J/(kg K))	1700	1190	1190
Thermal conductivity (W/(kg K))	100	211	91
Latent heat (J/kg)	–	3.98×10^5	–

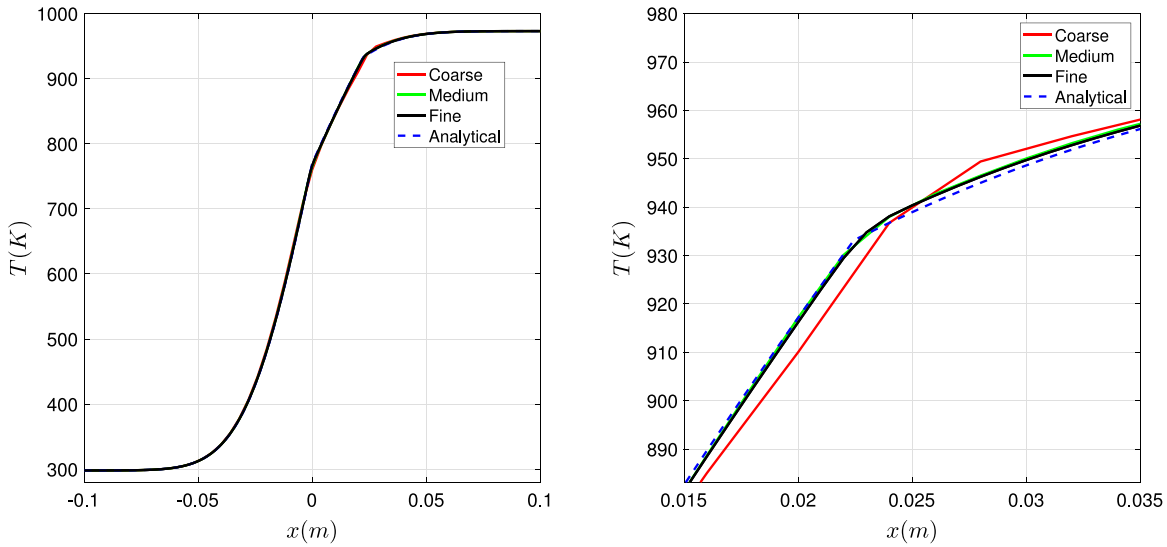

Fig. 4. The temperature distribution at $t = 10$ s. Left: temperature profile between -0.1 m $< x < 0.1$ m; Right: temperature profile of a zoomed-in window around the solid–liquid interface.

The analytical solution on an infinite domain, adapted from that in [87], is

$$\begin{aligned} x^* &= 7.095 \times 10^{-3}\sqrt{t}\, s \\ T_m &= 769.95 + 471.8 erf\left(\frac{96.69x}{\sqrt{t}}\right) K \\ T_s &= 769.95 + 360.2 erf\left(\frac{60.02x}{\sqrt{t}}\right) K \\ T_l &= 973.15 - 111.4 erfc\left(\frac{91.39x}{\sqrt{t}}\right) K, \end{aligned} \tag{46}$$

where x^* is the location of solid–liquid interface and T_m, T_s and T_l are the temperature distribution in the mold, solid phase and liquid phase, respectively.

We compute a 3D solution to this quasi-1D problem, using structured brick elements; 4×4 elements are used in the yz plane. A refinement study is performed by choosing three different element lengths ($h = 0.004, 0.002$ and 0.001) for the x-direction. The analytical solution at $t = 5$ s is used as the initial conditions for all simulations. Although the material is pure aluminum with a sharp phase transition at the melting temperature, to make the problem numerically computable, we artificially select liquidus and solidus temperatures to give a "mushy zone" interval of 10 K about the melting temperature (the size of this interval is further explored below).

Fig. 4 shows the temperature distribution at $t = 10$ s. Fig. 5 shows the time history of the position of the solid–liquid interface x^* after 5 s. The analytical solutions are also plotted for comparison. Intermittent error is observed in the position of the interface as the interface traverses discrete elements; this error is reduced when the mesh is refined. Convergence is observed among three different element lengths, and good agreement between the computed and analytical solutions is achieved.

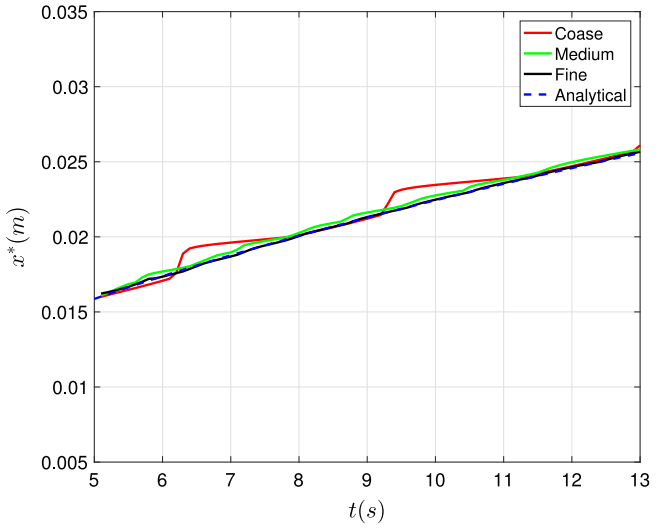

Fig. 5. Time history of the position of solid–liquid interface x^*.

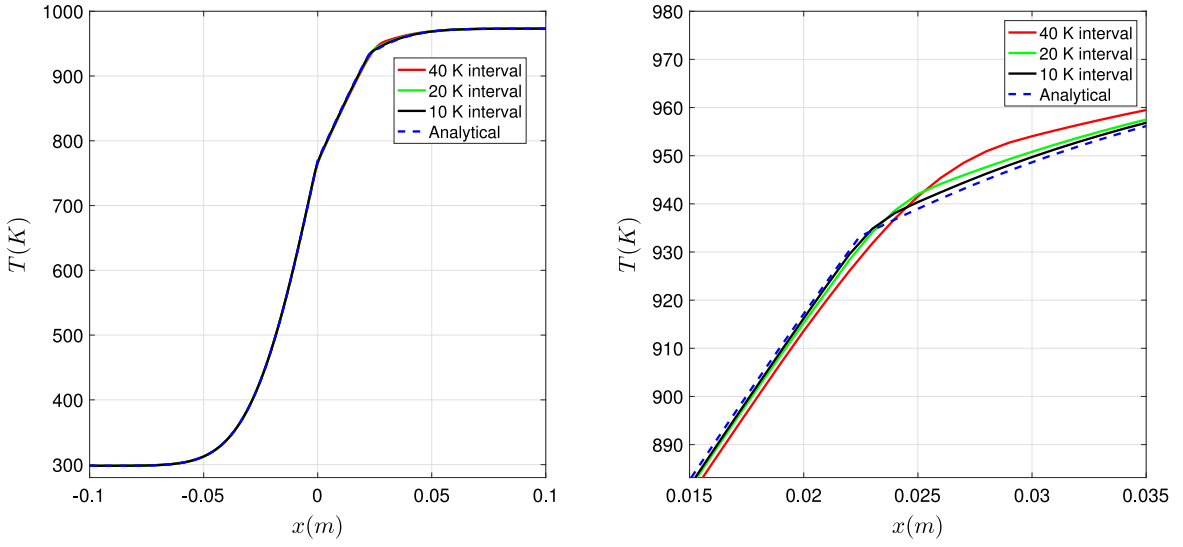

Fig. 6. The temperature distribution at $t = 10$ s using three different mushy zone temperature intervals. Left: temperature profile between -0.1 m $< x <$ 0.1 m; Right: temperature profile of a zoomed-in window around the solid–liquid interface.

The effect of the temperature interval of the mushy zone is also investigated. Fig. 6 shows the temperature distribution at $t = 10$ s for the fine mesh using 10 K, 20 K and 40 K for the artificial mushy zone temperature interval. We find that using a larger mushy zone temperature interval cannot resolve the solid–liquid interface very well. However, as we refine the temperature interval of the mushy zone, the computed results approach the analytical solution.

6.2. *Thermocapillary droplet migration*

In this section, the thermocapillary migration of a droplet in an ambient liquid with a linear initial temperature profile and without gravity is tested. The physical problem and the computational domain are sketched in Fig. 7. The simulations are performed on a 3D cube. The top and bottom surfaces are treated as no-slip walls and the temperature

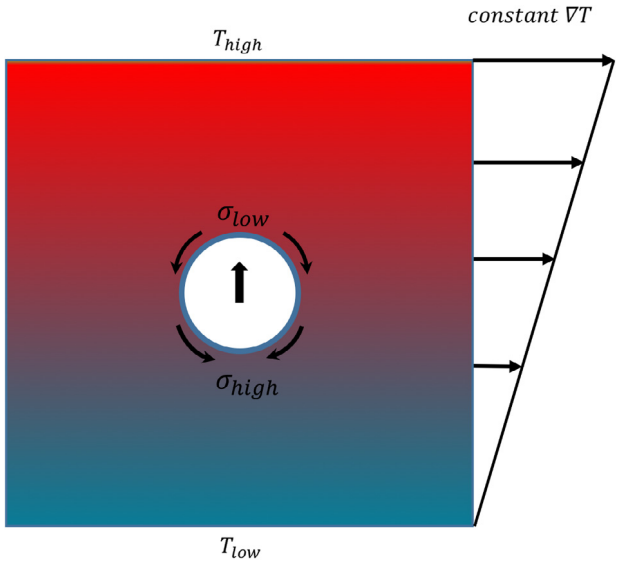

Fig. 7. Marangoni driven flows problem.

Table 2
Definition of material properties.

ρ	μ	κ	c_p
500 kg m^{-3}	2.4 × 10^{-2} Pa s	2.4 × 10^{-6} W m^{-1} K^{-1}	10^{-4} J kg^{-1} K^{-1}

Table 3
Definition of material properties.

σ_s	$\frac{d\sigma_s}{dT}$	$\lvert\nabla T\rvert$	a
0.01 N m^{-1}	−2 × 10^{-3} N m^{-1} K^{-1}	200 K m^{-1}	1.44 × 10^{-3} m

is fixed at the prescribed high (top) and low (bottom) temperatures. In the other directions, a no-penetration boundary condition is used for the velocity field and zero heat flux is used for the temperature field. The fluid is initially at rest and the initial temperature increases linearly from the cold bottom wall toward the hot top wall with given constant gradient. The material properties of the ambient fluid are given as in Table 2. The ratios of the material properties between the droplet and the ambient fluid are chosen to be 0.5. The surface tension coefficient, Marangoni coefficient, temperature gradient, and radius of the drop are given in Table 3. The problem can be characterized by Reynolds number, the Marangoni number and the capillary number, which are defined by

$$Re = \frac{\rho a W_r}{\mu}, \tag{47}$$

$$Ma = \frac{\rho c_p a W_r}{\kappa}, \tag{48}$$

$$Ca = \frac{\mu W_r}{\sigma_s}, \tag{49}$$

where W_r is the reference velocity, defined as $W_r = \frac{d\sigma_s}{dT}|\nabla T|a/\mu$. The material properties used give $Re = 0.72$, $Ma = 0.72$ and $Ca = 0.0576$, which are also used in the numerical simulations performed by Ma and Bothe [88] using the volume of fluid method.

The effect of domain size was studied in [88]. In the present work, the computational domain was chosen large enough to avoid wall effects according to the investigation in [88]. Three different meshes are employed to perform the simulations, with 16, 32 and 64 elements across the bubble diameter, respectively. Fig. 8 shows the

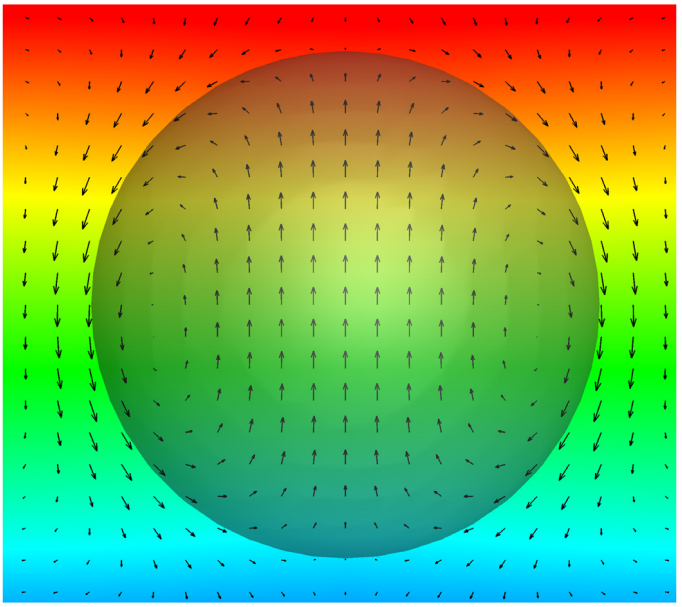

Fig. 8. Velocity vectors around the droplet on the medium mesh.

velocity vector on the $x = 0$ cross section for the medium mesh at the terminal stage. Due to the Marangoni effect, the surface tension is higher where the temperature is lower. Thus, around the bubble surface, the flow direction goes from higher temperature to lower temperature. A recirculation vortex is formed inside the bubble. This flow pattern was also observed in other numerical simulations, such as [89]. The time history of dimensionless migration velocity $W^* = W/W_r$ plotted against dimensionless time $t^* = tW_r/a$ is shown in Fig. 9 for the three meshes. Young [90] obtained an analytical expression of the dimensionless terminal migration velocity, given as $W^* = 2/[(2 + r_\kappa)(2 + 3r_\mu)]$, by assuming infinite domain and Stokes flow, and neglecting convective heat transport and deformation of the bubble. In the analytical expression, r_κ and r_μ denote the ratios of the thermal conductivities and dynamic viscosities between the bubble and the ambient fluid. The analytical solution and the numerical solution computed by Ma and Bothe [88] using the largest domain size are also plotted in Fig. 9 for comparison. A convergence trend and good agreement between different approaches are achieved.

6.3. Simulations of laser spot melt pool flows

In this section, the computational formulation is used to simulate laser spot melting, which was measured experimentally by Pitscheneder [91] and previously simulated by Saldi [48]. The material properties of the metal are based on steel (Fe–S system), and listed in Table 4. The setup of the computation is shown in Fig. 10. The computational domain is a cylinder with length of 14 mm and radius of 7 mm. The mesh is refined within a cylinder with length of 6 mm and radius of 3 mm in order to better capture the fluid dynamics of the melt pool. The element lengths and mesh statistics are summarized in Tables 5 and 6, and a cutaway view of the mesh is shown in Fig. 11. The initial condition is zero velocity and constant room temperature everywhere. On the lateral and bottom surfaces, no penetration and zero heat flux boundary conditions are adopted for the velocity field and the temperature field, respectively. A stationary laser heat flux with a top-hat profile is applied on the top surface of the computational domain. The prescribed flux on the top surface is

$$q_{in} = \begin{cases} \dfrac{\eta Q}{\pi R_{laser}^2} & \text{for } r \leqslant r_q \\ 0 & \text{for } r > r_q \end{cases} \tag{50}$$

where r is the radial coordinate in xy plane, $R_{laser} = 1.4$ mm is the equivalent laser radius, $Q = 5200$ W is the laser power, and $\eta = 0.13$ is the surface absorptivity.

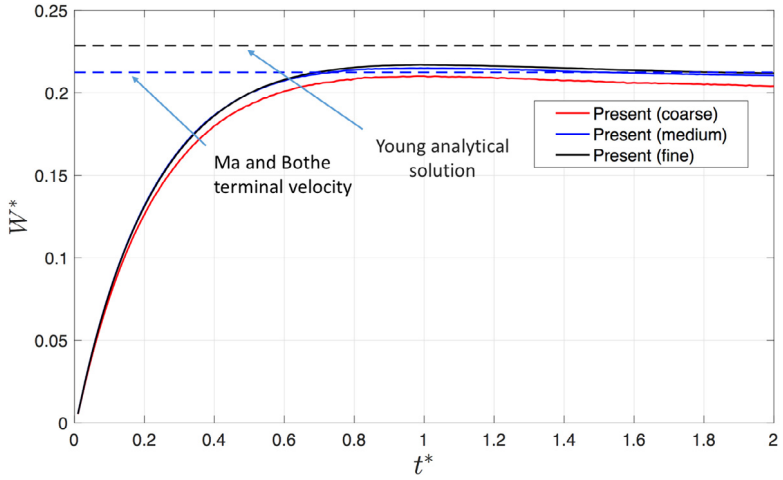

Fig. 9. Time history of migration velocity of different meshes. The analytical solution obtained by Young [90] is shown in black dash line. The terminal velocity obtained by Ma and Bothe [88] using largest domain size is shown in blue dash line. (For interpretation of the references to color in this figure legend, the reader is referred to the web version of this article.)

Table 4
Material properties of the metal.

Materials properties	Values	Units
Density of metal	8100	kg/m^3
Viscosity of metal	0.006	Pa s
Melting temperature of metal	1620	K
Solidus temperature	1610	K
Liquidus temperature	1630	K
Thermal conductivity of solid	22.9	J/(m s K)
Thermal conductivity of liquid	22.9	J/(m s K)
Specific heat of solid	627	J/(kg K)
Specific heat of liquid	723.14	J/(kg K)
Latent heat of melting	2.508×10^5	J/kg

In the present work, we make use of a flat free-surface assumption, which is also employed in [48,91]. To drive the flow, the following boundary condition is applied on the top surface:

$$(-p\boldsymbol{I} + 2\mu\nabla^S\boldsymbol{u}) \cdot \boldsymbol{n} = \frac{d\sigma_s}{dT}\left[\nabla T - (\nabla T \cdot \boldsymbol{n})\boldsymbol{n}\right]. \tag{51}$$

Pitscheneder et al. [91] also investigated the effect of sulfur activity on the melt pool flow and shape, thus the dependence of surface tension on temperature and sulfur activity needs to be known. The theoretical model by Sahoo et al. [92] is used in this paper and is given by

$$\frac{d\sigma_s}{dT} = \left.\frac{d\sigma_s}{dT}\right|_0 - R\tau_S ln(1 + Ka_i) - \frac{Ka_i}{1 + Ka_i}\frac{\tau_S(\Delta H^0 - \Delta H^M)}{T} \tag{52}$$

$$K = k_i \exp(\frac{-\Delta H^0}{RT}) \tag{53}$$

where $\left.\frac{d\sigma_s}{dT}\right|_0$ is the Marangoni coefficient for pure metal, τ_S is the surface excess at saturation, K is the equilibrium constant for segregation, k_i is the entropy factor, ΔH^0 is the standard heat of adsorption, ΔH^M is the partial molar enthalpy of species mixing in the solution, and a_i is sulfur activity in % weight. The values of these parameters for Fe–S system are listed in Table 7. In this paper, two sulfur activities with $a_i = 0.002$%-wt (20 ppm) and $a_i = 0.015$%-wt (150 ppm) are used. The corresponding Marangoni coefficient as a function of temperature is plotted in Fig. 14.

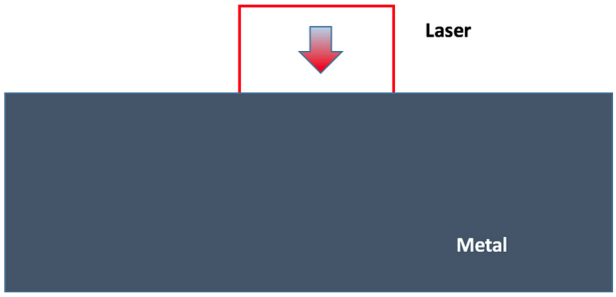

Fig. 10. Computational setup.

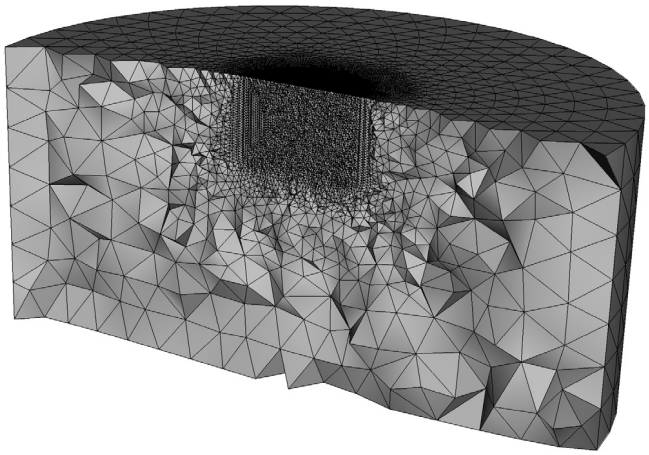

Fig. 11. Mesh of the computational domain.

Table 5
Element lengths employed in the simulation.

Outer cylinder	Refined cylinder	Units
2	0.012	mm

Table 6
Mesh statistics.

Total number of nodes	Total number of elements
164,939	965,041

Table 7
Parameters for Marangoni coefficient.

Parameters	Values	Units
$\frac{d\sigma_s}{dT}\|_0$	-5×10^{-4}	N/(m K)
τ_S	1.3×10^{-8}	kmole/m^2
k_i	3.18×10^{-3}	–
ΔH^0	-1.66×10^8	J/kmole
ΔH^M	0	J/kmole

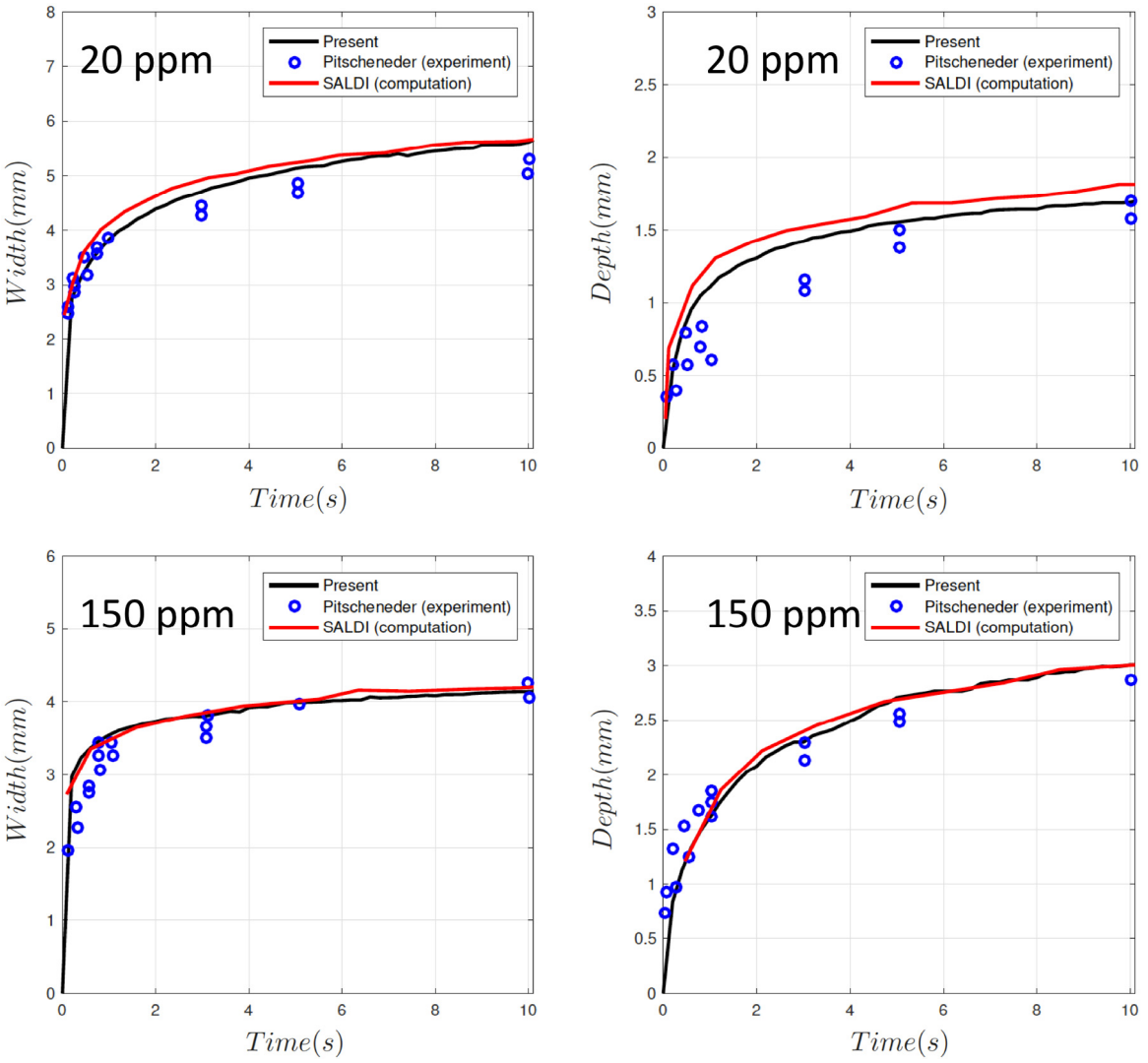

Fig. 12. Time history of the width and depth of the melt pool. The experimental measurements from [91] and the computational result from [48] using OpenFoam are also plotted for comparison.

Fig. 12 shows the time history of the depth and width of the melt pool of the two cases. The experimental measurements from Pitscheneder et al. [91] and the computational result from [48] using OpenFoam are also plotted for comparison. It can be seen that the computational result from this paper is slightly closer to the experimental result. The melt pool shape and velocity vectors in the melt pool at $t = 10$ s are shown in Fig. 13, where the background indicates the temperature. The melt pool shapes look quite similar to experimental image obtained by Pitscheneder et al. [91]. It can be also seen that the shapes of the two melt pools with different sulfur activity are quite different, where the melt pool with $a_i = 0.015$%-wt (150 ppm) has a larger depth and smaller width than that of the case with $a_i = 0.002$%-wt (20 ppm). For the case with $a_i = 0.002$%-wt (20 ppm), as shown in Fig. 14, the Marangoni coefficient $\frac{d\sigma_s}{dT}$ is mostly negative in the temperature range of the melt pool. This implies that surface tension in the hot zone (center of the melt pool) is lower than that in the melt pool edge, and the surface flow moves outward, resulting in a wide but shallow melt pool. In contrast, for the case with $a_i = 0.015$%-wt (150 ppm), $\frac{d\sigma_s}{dT}$ is mostly positive in the temperature range of the melt pool and an opposite direction of the melt pool flow is obtained, resulting in a narrow but deep melt pool.

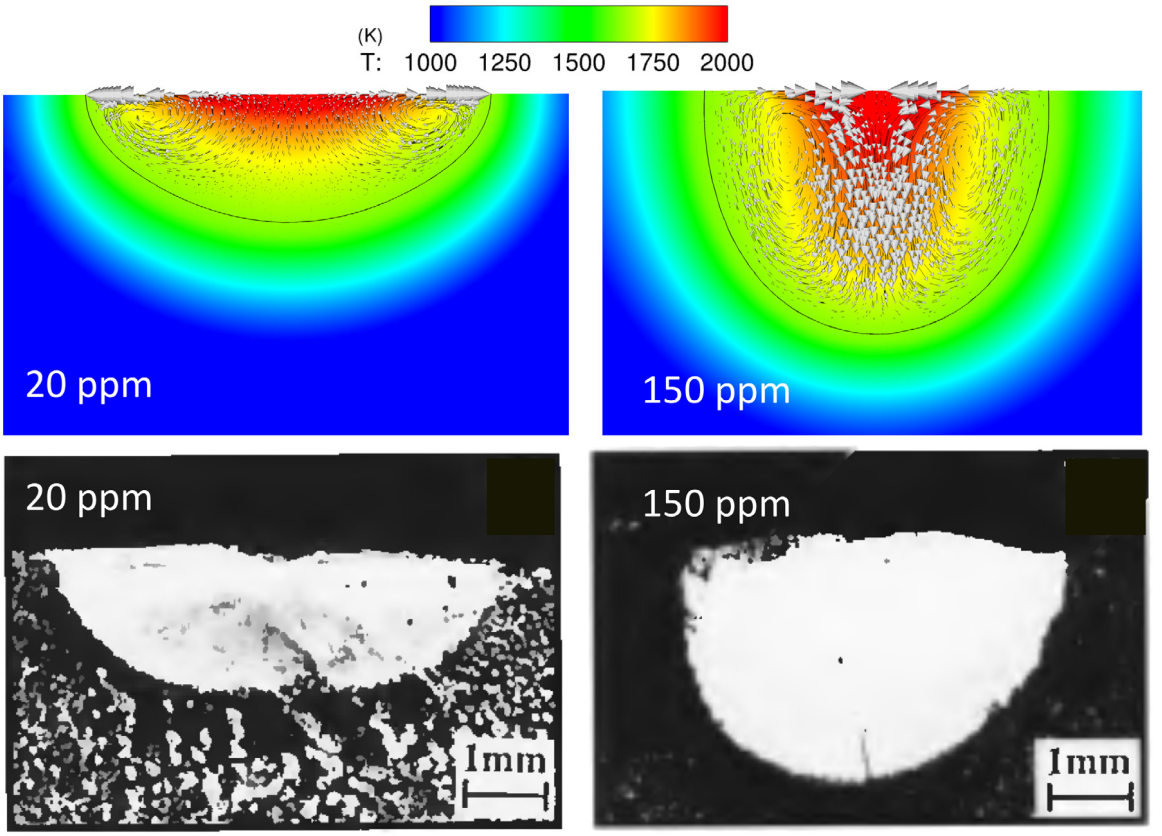

Fig. 13. Predicted shape (top) and experimental images [91] (bottom) for the melt pool in the two cases with 20 ppm (left) and 150 ppm (right) sulfur activity at 10 s. In the simulations, the predicted solid–liquid interface is indicated by the solid black line, while the background color denotes the temperature profile. (For interpretation of the references to color in this figure legend, the reader is referred to the web version of this article.)

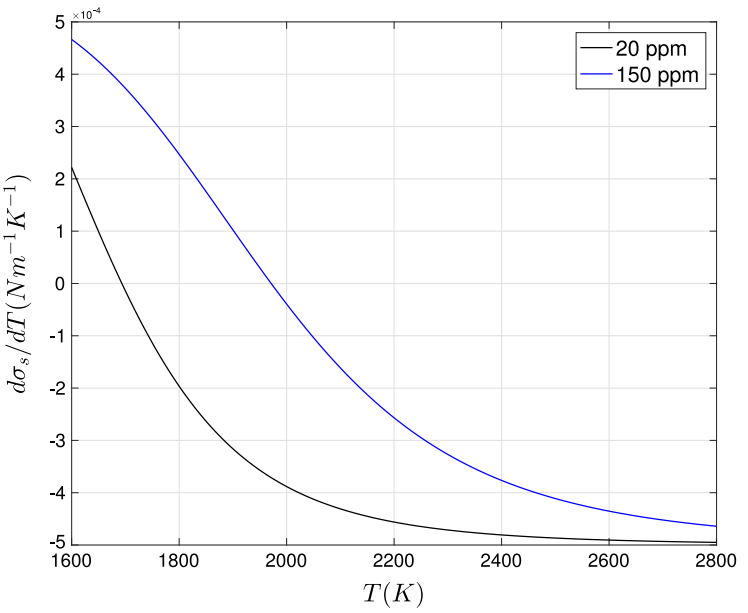

Fig. 14. Marangoni coefficient as a function of temperature for samples with 20 and 150 ppm sulfur activity.

Table 8
Material properties of the gas, surface tension and Marangoni coefficient.

Materials Properties	Values	Units
Density of gas	1.784	kg/m^3
Viscosity of gas	2.1×10^{-5}	Pa s
Thermal conductivity of gas	0.016	J/(m s K)
Specific heat of gas	520	J/(kg K)
Latent heat of melting	2.508×10^5	J/kg
Surface tension	1.8	N/m
Marangoni coefficient	-5×10^{-4}	N/(m K)

Table 9
Element lengths employed in the simulation.

Outer box	Refined box	Further refined box	Units
0.5	0.05	0.002	mm

Table 10
Mesh statistics.

Total number of nodes	Total number of elements
498,383	2922,576

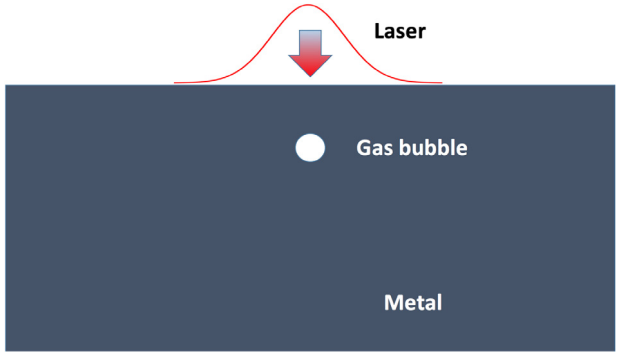

Fig. 15. Computational setup.

6.4. Melting and solidification of metal with a spherical bubble

An important source of defects in additively manufactured materials is the trapping of voids or bubbles during solidification, which is difficult to model or observe experimentally. To demonstrate the capability of the proposed formulation to capture this phenomenon, the melting and solidification of a metal with a spherical bubble inside is simulated. In this simulation, all the functionalities of the proposed framework are enabled. Metal are based on steel (Fe–S system) with zero sulfur activity. Thus the Marangoni coefficient is constant and negative in this case. The material properties of the metal and gas, surface tension and Marangoni coefficient are listed in Tables 4 and 8. The setup of the computation is shown in Fig. 15. The metal domain is a cubical box with side length 5 mm, with a spherical bubble located on the central vertical axis under the top surface. The gas bubble is initially located at (0,0,4.5367) mm with radius of 0.022 mm. A mesh-refined region with dimensions of 2 mm $\times$ 2 mm $\times$ 1.3333 mm is included to better capture the dynamics of the melt pool. A further refined region with dimensions of 0.08 mm $\times$ 0.08 mm $\times$ 0.2 mm is designed to better resolve the deformation of the gas bubble. A snapshot of the mesh is shown in Fig. 16. The element lengths and mesh statistics are summarized in Table 9 and Table 10. The same initial and boundary conditions used in the previous section are employed here again, except at the top surface, at which, a non-moving laser heat flux with a

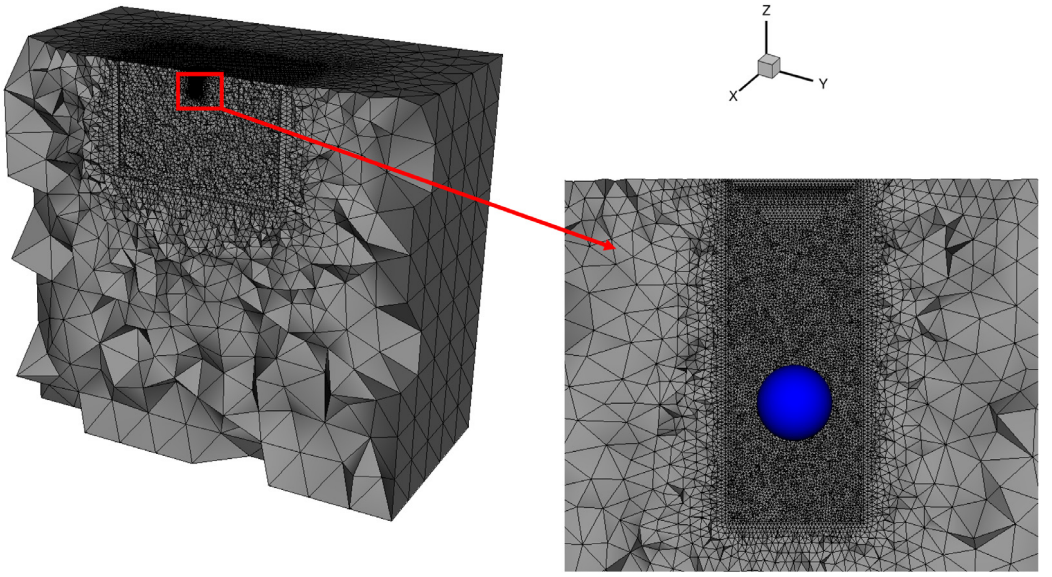

Fig. 16. Mesh of the computational domain.

Gaussian profile is applied and specified as follows:

$$q_{in} = \frac{2\eta Q}{\pi R_{laser}^2} e^{-2(\frac{r}{R_{laser}})^2} \tag{54}$$

where $R_{laser} = 0.5657$ mm, $Q = 1875$ W, and $\eta = 0.13$ are used. In the simulation, the laser is turned on immediately once the simulation is started and remains active until $t = 4.475 \times 10^{-3}$ s, when the solid–liquid interface just passes the bubble. After this point, to promote solidification and demonstrate trapping of the bubble, a fixed temperature of 600 K is prescribed on the top surface. The computation is performed until the entire metal is re-solidified.

Fig. 17 shows 6 snapshots of the bubble shape and temperature at the central plane ($x = 0$) of the domain. Before 0.003 s, the gas bubble is trapped in the solid and does not move at all. After the surrounding metal has been melted, the bubble starts to deform. In the time interval between 0.003 s and 0.0043 s, the upper part of the bubble is in the liquid and begins to rise, while the lower part is still in the solid and lags behind; thus the total average rising speed of the bubble is slow. After 0.0043 s, as the solid surrounding the bubble is totally melted into liquid, the bubble deforms dramatically and rises toward to the top surface. Fig. 18 shows 6 snapshots of the velocity vectors in the melt pool at the central plane ($x = 0$) of the domain, with background color denoting the velocity magnitude. Since we are using a negative Marangoni coefficient, the flow at the surface goes from high temperature to low temperature. Thus a recirculation region (a toroidal vortex in this axisymmetric flow) is formed in the melt pool. After the bubble is fully in the liquid phase, another vortex is formed around the gas bubble. After the laser is turned off, the metal starts to re-solidify. Since a very low temperature is utilized for the top surface, a closed solid–liquid interface is formed and surrounds the rising bubble. In the end, the entire material is re-solidified, the bubble is trapped in the solid. Fig. 19 shows the time history of the position of the center of the gas bubble. From this plot, we can also see that the gas bubble barely moves until it is released from the solid phase. After the metal around the bubble is totally melted, the bubble is quickly carried to the surface by buoyancy and the upward central vertical velocity driven by the Marangoni effect. This is also supported by Fig. 18 (d and e), from which we can clearly see that the velocity magnitude around the bubble is significantly higher than the velocity magnitude in other regions of the melt pool. Once the bubble meets the solid–liquid interface, the average position of the bubble decreases slightly, and then stays as a constant as the remaining metal solidifies.

7. Conclusions

In this paper, a fully coupled formulation for thermal multi-phase flows is developed. The formulation is based on the level set technique and RBVMS, and incorporates phase transition, surface tension and Marangoni effect. A

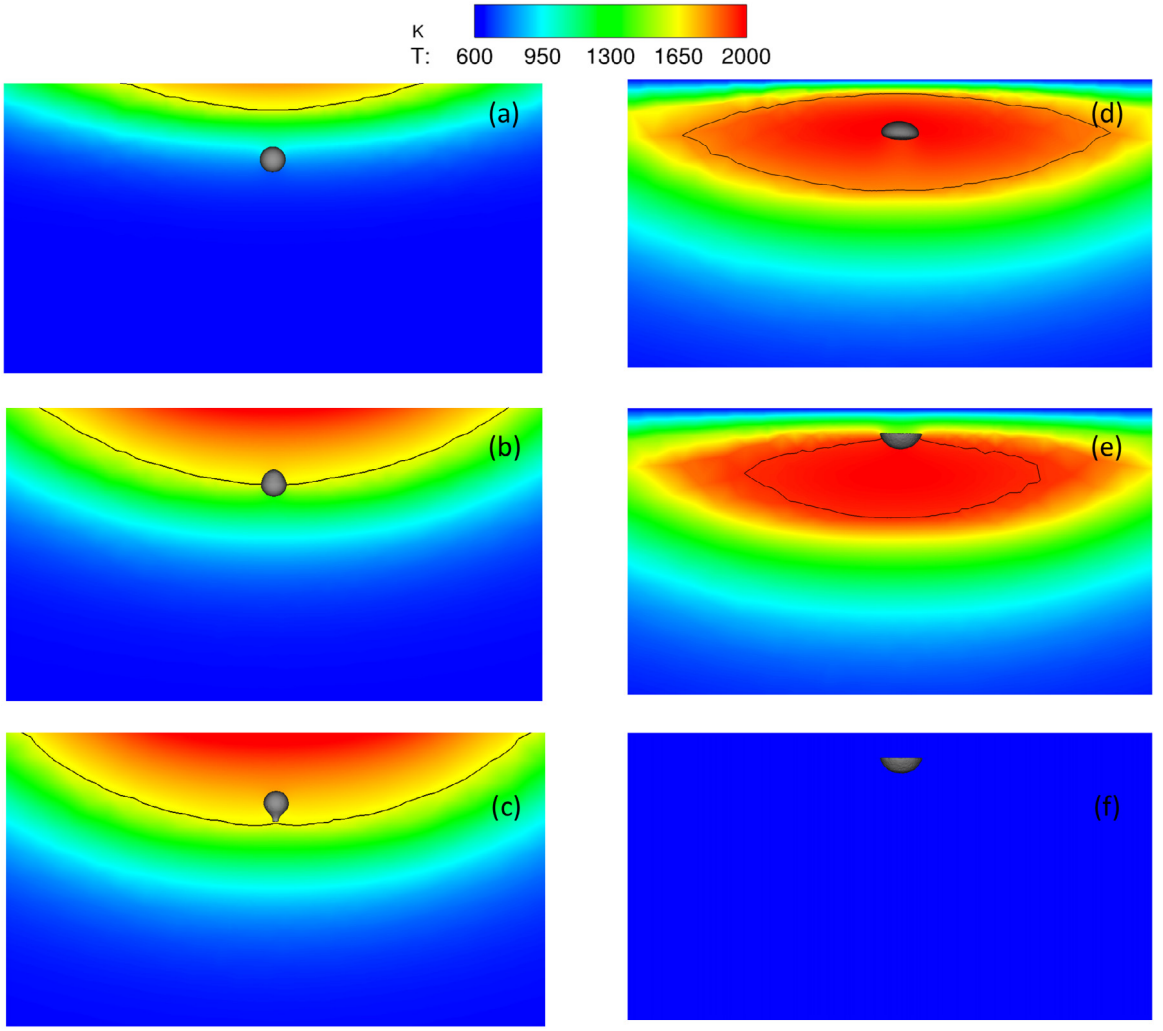

Fig. 17. Temperature profile. The solid–liquid interface is indicated by the solid black line. (a) $t = 1.225 \times 10^{-3}$ s; (b) $t = 3.4250 \times 10^{-3}$ s ; (c) $t = 4.5125 \times 10^{-3}$ s; (d) $t = 4.52 \times 10^{-3}$ s; (e) $t = 4.608 \times 10^{-3}$ s. (f) $t = 1 \times 10^{-2}$ s.

fully coupled solution strategy based on FGMRES is developed to achieve robust simulations. Numerical evidence is presented in the first two computational cases, including mesh refinement studies and validation using analytical and computational results from the literature, that support the accuracy of the proposed approach. The last numerical example illustrates the power of the proposed methodology with all the functionalities enabled by applying the formulation to a challenging problem involving the fluid dynamics of gas and condensed phases, solid–liquid phase transition, bubble deformation, bubble rise in a melt pool, and bubble trapping in the re-solidified material.

To the best knowledge of the authors, this is the first FEM-based thermal multi-phase flows formulation with the capability to capture phase transition, interfacial forces, and the dynamics of gas, liquid and solid phases simultaneously. Through the four numerical examples presented, the formulation has been proved to be accurate and robust, and can be widely applied to simulate complex gas–liquid–solid systems such as those in additive manufacturing processes, which are difficult to model by current numerical methods.

Acknowledgments

The support of this research by the National Science Foundation under CPS-1646592 for J. Yan and G.J.Wagner and a Graduate Research Fellowship under DGE-1324585 for S.E. Lin is gratefully acknowledged.

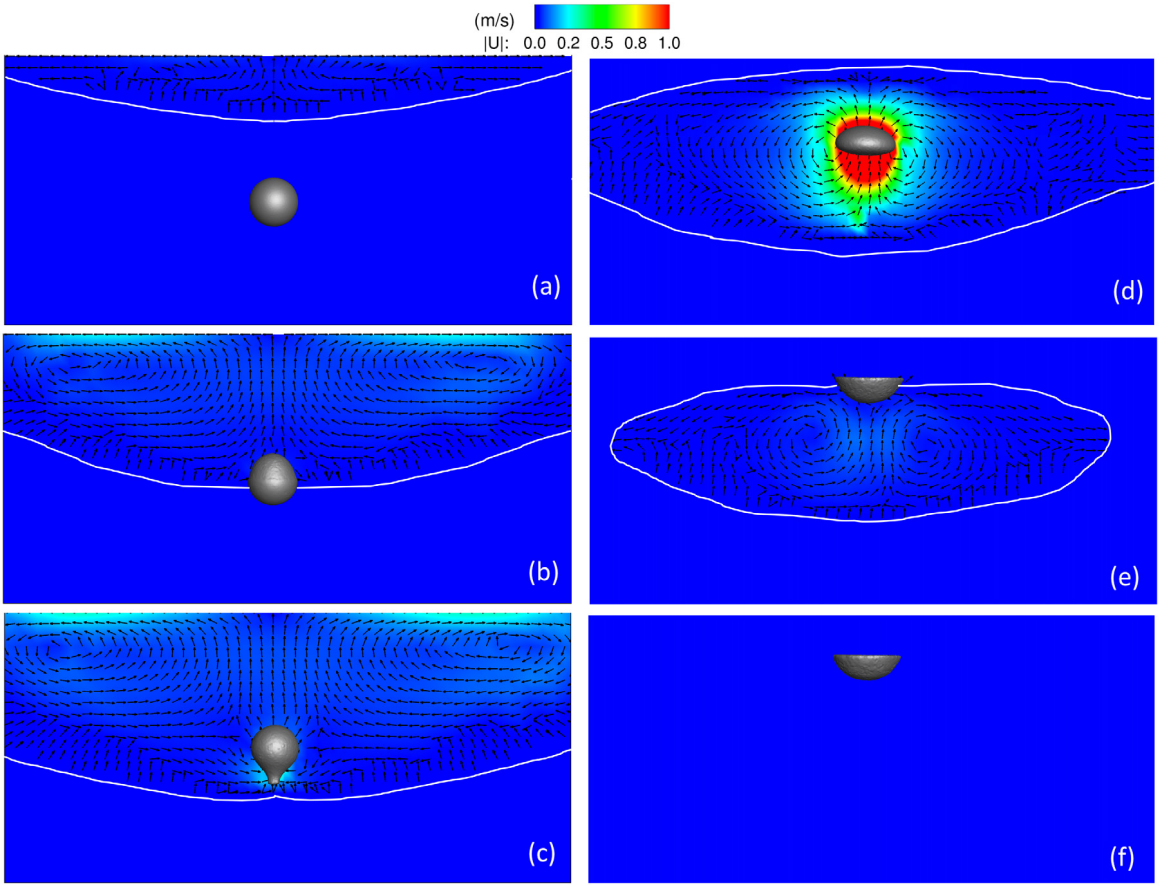

Fig. 18. Velocity vectors in the melt pool. The solid–liquid interface is indicated by the solid white line. The background color indicates the velocity magnitude. (a) $t = 1.225 \times 10^{-3}$ s; (b) $t = 3.4250 \times 10^{-3}$ s; (c) $t = 4.5125 \times 10^{-3}$ s; (d) $t = 4.52 \times 10^{-3}$ s; (e) $t = 4.608 \times 10^{-3}$ s. (f) $t = 1 \times 10^{-2}$ s. (For interpretation of the references to color in this figure legend, the reader is referred to the web version of this article.)

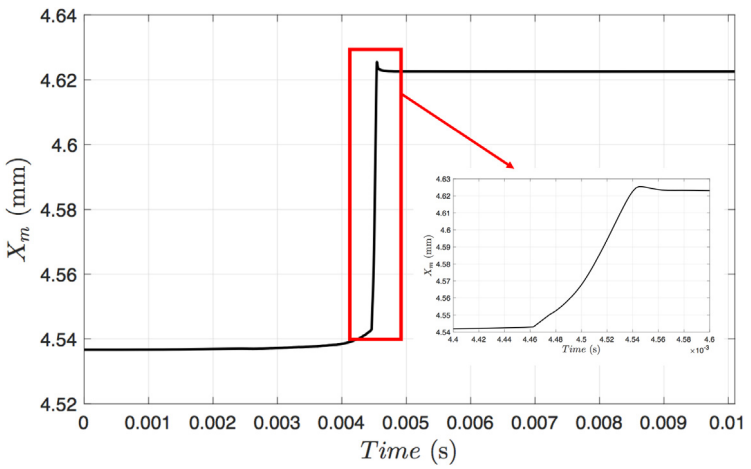

Fig. 19. Time history of the bubble center.

References

[1] Andrea Prosperetti, Lawrence A. Crum, Kerry W. Commander, Nonlinear bubble dynamics, J. Acoust. Soc. Am. 83 (2) (1988) 502–514.
[2] Milton S. Plesset, Andrea Prosperetti, Bubble dynamics and cavitation, Annu. Rev. Fluid Mech. 9 (1) (1977) 145–185.
[3] Andrea Prosperetti, Vapor bubbles, Annu. Rev. Fluid Mech. 49 (2017) 221–248.
[4] Wentao Yan, Wenjun Ge, Jacob Smith, Stephen Lin, Orion L. Kafka, Feng Lin, Wing Kam Liu, Multi-scale modeling of electron beam melting of functionally graded materials, Acta Mater. 115 (2016) 403–412.
[5] Wentao Yan, Wenjun Ge, Ya Qian, Stephen Lin, Bin Zhou, Wing Kam Liu, Feng Lin, Gregory J. Wagner, Multi-physics modeling of single/multiple-track defect mechanisms in electron beam selective melting, Acta Mater. 134 (2017) 324–333.
[6] Ramon Codina, Javier Principe, Dynamic subscales in the finite element approximation of thermally coupled incompressible flows, Internat. J. Numer. Methods Fluids 54 (6–8) (2007) 707–730.
[7] Ramon Codina, Noel Hernández, Approximation of the thermally coupled MHD problem using a stabilized finite element method, J. Comput. Phys. 230 (4) (2011) 1281–1303.
[8] B.A. Schrefler, R. Codina, F. Pesavento, J. Principe, Thermal coupling of fluid flow and structural response of a tunnel induced by fire, Internat. J. Numer. Methods Engrg. 87 (1–5) (2011) 361–385.
[9] Tayfun E. Tezduyar, Srinivas Ramakrishnan, Sunil Sathe, Stabilized formulations for incompressible flows with thermal coupling, Internat. J. Numer. Methods Fluids 57 (9) (2008) 1189–1209.
[10] Kenji Takizawa, Tayfun E. Tezduyar, Takashi Kuraishi, Multiscale space–time methods for thermo-fluid analysis of a ground vehicle and its tires, Math. Models Methods Appl. Sci. 25 (12) (2015) 2227–2255.
[11] Kenji Takizawa, Tayfun E. Tezduyar, Takashi Kuraishi, Shinichiro Tabata, Hirokazu Takagi, Computational thermo-fluid analysis of a disk brake, Comput. Mech. 57 (6) (2016) 965–977.
[12] Andrea Prosperetti, Grétar Tryggvason, Computational Methods for Multiphase Flow, Cambridge University Press, 2009.
[13] T.E. Tezduyar, Finite element methods for flow problems with moving boundaries and interfaces, Arch. Comput. Methods Eng. 8 (2001) 83–130. http://dx.doi.org/10.1007/BF02897870.
[14] Salih Ozen Unverdi, Grétar Tryggvason, A front-tracking method for viscous, incompressible, multi-fluid flows, J. Comput. Phys. 100 (1) (1992) 25–37.
[15] J.P. Best, The formation of toroidal bubbles upon the collapse of transient cavities, J. Fluid Mech. 251 (1993) 79–107.
[16] T.J.R. Hughes, W.K. Liu, T.K. Zimmermann, Lagrangian–Eulerian finite element formulation for incompressible viscous flows, Comput. Methods Appl. Mech. Engrg. 29 (1981) 329–349.
[17] T.E. Tezduyar, M. Behr, J. Liou, A new strategy for finite element computations involving moving boundaries and interfaces –the deforming-spatial-domain/space–time procedure: I. The concept and the preliminary numerical tests, Comput. Methods Appl. Mech. Engrg. 94 (3) (1992) 339–351. http://dx.doi.org/10.1016/0045-7825(92)90059-S.
[18] T.E. Tezduyar, M. Behr, S. Mittal, J. Liou, A new strategy for finite element computations involving moving boundaries and interfaces –the deforming-spatial-domain/space–time procedure: II. Computation of free-surface flows, two-liquid flows, and flows with drifting cylinders, Comput. Methods Appl. Mech. Engrg. 94 (3) (1992) 353–371. http://dx.doi.org/10.1016/0045-7825(92)90060-W.
[19] Jinsong Hua, Jan F. Stene, Ping Lin, Numerical simulation of 3D bubbles rising in viscous liquids using a front tracking method, J. Comput. Phys. 227 (6) (2008) 3358–3382.
[20] C.W. Hirt, B.D. Nichols, Volume of fluid (VOF) method for the dynamics of free boundaries, J. Comput. Phys. 39 (1981) 201–225.
[21] David Jacqmin, Calculation of two-phase Navier–Stokes flows using phase-field modeling, J. Comput. Phys. 155 (1) (1999) 96–127.
[22] Ju Liu, Thermodynamically Consistent Modeling and Simulation of Multiphase Flows (Ph.D. thesis).
[23] Jesus Bueno, Hector Gomez, Liquid-vapor transformations with surfactants. Phase-field model and isogeometric analysis, J. Comput. Phys. 321 (2016) 797–818.
[24] Hector Gomez, Alessandro Reali, Giancarlo Sangalli, Accurate, efficient, and (iso) geometrically flexible collocation methods for phase-field models, J. Comput. Phys. 262 (2014) 153–171.
[25] Ju Liu, Chad M. Landis, Hector Gomez, Thomas J.R. Hughes, Liquid–vapor phase transition: Thermomechanical theory, entropy stable numerical formulation, and boiling simulations, Comput. Methods Appl. Mech. Engrg. 297 (2015) 476–553.
[26] Pengtao Yue, James J. Feng, Chun Liu, Jie Shen, A diffuse-interface method for simulating two-phase flows of complex fluids, J. Fluid Mech. 515 (2004) 293–317.
[27] Luz Amaya-Bower, Taehun Lee, Single bubble rising dynamics for moderate Reynolds number using lattice Boltzmann method, Comput. & Fluids 39 (7) (2010) 1191–1207.
[28] E. Shirani, N. Ashgriz, J. Mostaghimi, Interface pressure calculation based on conservation of momentum for front capturing methods, J. Comput. Phys. 203 (1) (2005) 154–175.
[29] Mark Sussman, Ann S. Almgren, John B. Bell, Phillip Colella, Louis H. Howell, Michael L. Welcome, An adaptive level set approach for incompressible two-phase flows, J. Comput. Phys. 148 (1) (1999) 81–124.
[30] Mark Sussman, Peter Smereka, Stanley Osher, A level set approach for computing solutions to incompressible two-phase flow, J. Comput. Phys. 114 (1) (1994) 146–159.
[31] James A. Sethian, A fast marching level set method for monotonically advancing fronts, Proc. Natl. Acad. Sci. 93 (4) (1996) 1591–1595.
[32] Stanley Osher, Ronald Fedkiw, Level Set Methods and Dynamic Implicit Surfaces, Vol. 153, Springer Science & Business Media, 2006.
[33] J. Yan, S. Lin, Y. Bazilevs, G. Wagner, Isogeometric analysis of multi-phase flows with surface tension and with application to dynamics of rising bubbles, Comput. Fluids (2018) Submitted.
[34] Sunitha Nagrath, Kenneth E. Jansen, Richard T. Lahey, Computation of incompressible bubble dynamics with a stabilized finite element level set method, Comput. Methods Appl. Mech. Engrg. 194 (42) (2005) 4565–4587.

[35] Manoj Kumar Tripathi, Kirti Chandra Sahu, Rama Govindarajan, Dynamics of an initially spherical bubble rising in quiescent liquid, Nature Commun. 6 (2015).
[36] M. van Sint Annaland, N.G. Deen, J.A.M. Kuipers, Numerical simulation of gas bubbles behaviour using a three-dimensional volume of fluid method, Chem. Eng. Sci. 60 (11) (2005) 2999–3011.
[37] Juan M. Gimenez, Norberto M. Nigro, Sergio R. Idelsohn, Eugenio Oñate, Surface tension problems solved with the particle finite element method using large time-steps, Comput. & Fluids (2016).
[38] J. Yan, X. Deng, A. Korobenko, Y. Bazilevs, Free-surface flow modeling and simulation of horizontal-axis tidal-stream turbines, Comput. & Fluids (2016).
[39] J. Yan, A. Korobenko, X. Deng, Y. Bazilevs, Computational free-surface fluid–structure interaction with application to floating offshore wind turbines, Comput. & Fluids (2016).
[40] I. Akkerman, Y. Bazilevs, C.E. Kees, M.W. Farthing, Isogeometric analysis of free-surface flow, J. Comput. Phys. 230 (2011) 4137–4152.
[41] I. Akkerman, Y. Bazilevs, D.J. Benson, M.W. Farthing, C.E. Kees, Free-surface flow and fluid–object interaction modeling with emphasis on ship hydrodynamics, J. Appl. Mech. 79 (2012) 010905.
[42] Haiyan Zhao, Wenchong Niu, Bin Zhang, Yongping Lei, Masaru Kodama, Takashi Ishide, Modelling of keyhole dynamics and porosity formation considering the adaptive keyhole shape and three-phase coupling during deep-penetration laser welding, J. Phys. D: Appl. Phys. 44 (48) (2011) 485302.
[43] Wenda Tan, Neil S. Bailey, Yung C. Shin, Investigation of keyhole plume and molten pool based on a three-dimensional dynamic model with sharp interface formulation, J. Phys. D: Appl. Phys. 46 (5) (2013) 055501.
[44] Won-Ik Cho, Suck-Joo Na, Claus Thomy, Frank Vollertsen, Numerical simulation of molten pool dynamics in high power disk laser welding, J. Mater Process. Technol. 212 (1) (2012) 262–275.
[45] Shengyong Pang, Liliang Chen, Jianxin Zhou, Yajun Yin, Tao Chen, A three-dimensional sharp interface model for self-consistent keyhole and weld pool dynamics in deep penetration laser welding, J. Phys. D: Appl. Phys. 44 (2) (2010) 025301.
[46] Hyungson Ki, Jyoti Mazumder, Pravansu S Mohanty, Modeling of laser keyhole welding: Part I. Mathematical modeling, numerical methodology, role of recoil pressure, multiple reflections, and free surface evolution, Metall. Mater. Trans. A 33 (6) (2002) 1817–1830.
[47] Chinnapat Panwisawas, Chunlei Qiu, Magnus J. Anderson, Yogesh Sovani, Richard P. Turner, Moataz M. Attallah, Jeffery W. Brooks, Hector C. Basoalto, Mesoscale modelling of selective laser melting: Thermal fluid dynamics and microstructural evolution, Comput. Mater. Sci. 126 (2017) 479–490.
[48] Zaki Saptari Saldi, Marangoni Driven Free Surface Flows in Liquid Weld Pools (Ph.D. disseration), Delft University of Technology, 2012.
[49] Y. Bazilevs, V.M. Calo, J.A. Cottrell, T.J.R. Hughes, A. Reali, G. Scovazzi, Variational multiscale residual-based turbulence modeling for large eddy simulation of incompressible flows, Comput. Methods Appl. Mech. Engrg. 197 (2007) 173–201.
[50] Y. Bazilevs, I. Akkerman, Large eddy simulation of turbulent Taylor–Couette flow using isogeometric analysis and the residual–based variational multiscale method, J. Comput. Phys. 229 (2010) 3402–3414.
[51] Y. Bazilevs, J. Yan, M. de Stadler, S. Sarkar, Computation of the flow over a sphere at Re = 3700: A comparison of uniform and turbulent inflow conditions, J. Appl. Mech. 81 (12) (2014) 121003.
[52] Roozbeh Golshan, Andrés E. Tejada-Martínez, Mario Juha, Yuri Bazilevs, Large-eddy simulation with near-wall modeling using weakly enforced no-slip boundary conditions, Comput. & Fluids 118 (2015) 172–181.
[53] Andrés E. Tejada-Martínez, Ido Akkerman, Yuri Bazilevs, Large-eddy simulation of shallow water Langmuir turbulence using isogeometric analysis and the residual-based variational multiscale method, J. Appl. Mech. 79 (1) (2012) 010909.
[54] Fei Xu, Dominik Schillinger, David Kamensky, Vasco Varduhn, Chenglong Wang, Ming-Chen Hsu, The tetrahedral finite cell method for fluids: Immersogeometric analysis of turbulent flow around complex geometries, Comput. & Fluids (2015).
[55] Timo M. van Opstal, Jinhui Yan, Chris Coley, John A. Evans, Trond Kvamsdal, Yuri Bazilevs, Isogeometric divergence-conforming variational multiscale formulation of incompressible turbulent flows, Comput. Methods Appl. Mech. Engrg. (2016).
[56] J. Yan, A. Korobenko, A.E. Tejada-Martínez, R. Golshan, Y. Bazilevs, A new variational multiscale formulation for stratified incompressible turbulent flows, Comput. & Fluids (2016).
[57] Y. Bazilevs, K. Kamran, G. Moutsanidis, D.J. Benson, E. Oñate, A new formulation for air-blast fluid–structure interaction using an immersed approach. Part I: basic methodology and FEM-based simulations, Comput. Mech. (2017) 1–18.
[58] Y. Bazilevs, G. Moutsanidis, J. Bueno, K. Kamran, D. Kamensky, M.C. Hillman, H. Gomez, J.S. Chen, A new formulation for air-blast fluid–structure interaction using an immersed approach: part II—coupling of IGA and meshfree discretizations, Comput. Mech. (2017) 1–16.
[59] J.U. Brackbill, Douglas B. Kothe, Charles Zemach, A continuum method for modeling surface tension, J. Comput. Phys. 100 (2) (1992) 335–354.
[60] J. Yan, B. Augier, A. Korobenko, J. Czarnowski, G. Ketterman, Y. Bazilevs, Fsi modeling of a propulsion system based on compliant hydrofoils in a tandem configuration, Comput. & Fluids (2015).
[61] C.C. Long, A.L. Marsden, Y. Bazilevs, Fluid–structure interaction simulation of pulsatile ventricular assist devices, Comput. Mech. 52 (2013) 971–981. http://dx.doi.org/10.1007/s00466-013-0858-3.
[62] Yuri Bazilevs, Kenji Takizawa, Tayfun E. Tezduyar, Computational Fluid–Structure Interaction: Methods and Applications, John Wiley & Sons, 2013.
[63] V.R. Voller, M. Cross, N.C. Markatos, An enthalpy method for convection/diffusion phase change, Internat. J. Numer. Methods Engrg. 24 (1) (1987) 271–284.
[64] V.R. Voller, C.R. Swaminathan, Brian G. Thomas, Fixed grid techniques for phase change problems: a review, Internat. J. Numer. Methods Engrg. 30 (4) (1990) 875–898.
[65] A.N. Brooks, T.J.R. Hughes, Streamline upwind/Petrov-Galerkin formulations for convection dominated flows with particular emphasis on the incompressible Navier-Stokes equations, Comput. Methods Appl. Mech. Engrg. 32 (1982) 199–259.

[66] Ming-Chen Hsu, Y. Bazilevs, V.M. Calo, T.E. Tezduyar, T.J.R. Hughes, Improving stability of stabilized and multiscale formulations in flow simulations at small time steps, Comput. Methods Appl. Mech. Engrg. 199 (2010) 828–840. http://dx.doi.org/10.1016/j.cma.2009.06.019.
[67] K. Takizawa, T.E. Tezduyar, T. Kuraishi, Multiscale space–time methods for thermo-fluid analysis of a ground vehicle and its tires, Math. Models Methods Appl. Sci. 25 (12) (2015) 2227–2255.
[68] K. Takizawa, T.E. Tezduyar, S. McIntyre, N. Kostov, R. Kolesar, C. Habluetzel, Space–time VMS computation of wind-turbine rotor and tower aerodynamics, Comput. Mech. 53 (2014) 1–15. http://dx.doi.org/10.1007/s00466-013-0888-x.
[69] T. Tezduyar, Stabilization parameters and local length scales in SUPG and PSPG formulations, in: Proceedings of the Fifth World Congress on Computational Mechanics, Vienna, Austria, 2002, Paper-ID: 81508. On-line publication: http://wccm.tuwien.ac.at/.
[70] T. Tezduyar, Interface-tracking and interface-capturing techniques for computation of moving boundaries and interfaces, in: Proceedings of the Fifth World Congress on Computational Mechanics, Vienna, Austria, 2002, Paper-ID: 81513. On-line publication: http://wccm.tuwien.ac.at/.
[71] T.E. Tezduyar, S. Sathe, R. Keedy, K. Stein, Space–time finite element techniques for computation of fluid–structure interactions, Comput. Methods Appl. Mech. Engrg. 195 (2006) 2002–2027. http://dx.doi.org/10.1016/j.cma.2004.09.014.
[72] Isaac Harari, Thomas J.R. Hughes, What are c and h? Inequalities for the analysis and design of finite element methods, Comput. Methods Appl. Mech. Engrg. 97 (2) (1992) 157–192.
[73] C.E. Kees, I. Akkerman, M.W. Farthing, Y. Bazilevs, A conservative level set method suitable for variable-order approximations and unstructured meshes, J. Comput. Phys. 230 (2011) 4536–4558.
[74] I. Akkerman, J. Dunaway, J. Kvandal, J. Spinks, Y. Bazilevs, Toward free-surface modeling of planing vessels: simulation of the Fridsma hull using ALE-VMS, Comput. Mech. 50 (2012) 719–727.
[75] I. Akkerman, Y. Bazilevs, Chris E. Kees, Matthew W. Farthing, Isogeometric analysis of free-surface flow, J. Comput. Phys. 230 (11) (2011) 4137–4152.
[76] T.J.R. Hughes, J.A. Cottrell, Y. Bazilevs, Isogeometric analysis: CAD, finite elements, NURBS, exact geometry, and mesh refinement, Comput. Methods Appl. Mech. Engrg. 194 (2005) 4135–4195.
[77] J.A. Cottrell, T.J.R. Hughes, Y. Bazilevs, Isogeometric Analysis. Toward Integration of CAD and FEA, Wiley, 2009.
[78] Kensuke Yokoi, A density-scaled continuum surface force model within a balanced force formulation, J. Comput. Phys. 278 (2014) 221–228.
[79] J. Chung, G.M. Hulbert, A time integration algorithm for structural dynamics with improved numerical dissipation: The generalized-α method, J. Appl. Mech. 60 (1993) 371–375.
[80] Kenneth E. Jansen, Christian H. Whiting, Gregory M. Hulbert, A generalized-α method for integrating the filtered Navier–Stokes equations with a stabilized finite element method, Comput. Methods Appl. Mech. Engrg. 190 (3) (2000) 305–319.
[81] Dana A. Knoll, David E. Keyes, Jacobian-free Newton–Krylov methods: a survey of approaches and applications, J. Comput. Phys. 193 (2) (2004) 357–397.
[82] Z. Johan, T.J.R. Hughes, F. Shakib, A globally convergent matrix-free algorithm for implicit time-marching schemes arising in finite element analysis in fluids, Comput. Methods Appl. Mech. Engrg. 87 (1991) 281–304.
[83] Z. Johan, K.K. Mathur, S.L. Johnsson, T.J.R. Hughes, A case study in parallel computation: Viscous flow around an onera M6 wing, Internat. J. Numer. Methods Fluids 21 (1995) 877–884.
[84] T.E. Tezduyar, Finite element methods for fluid dynamics with moving boundaries and interfaces, in: E. Stein, R. De Borst, T.J.R. Hughes (Eds.), Encyclopedia of Computational Mechanics, in: Fluids, vol. 3, John Wiley & Sons, 2004 (Chapter 17).
[85] T.E. Tezduyar, Finite elements in fluids: Stabilized formulations and moving boundaries and interfaces, Comput. & Fluids 36 (2007) 191–206. http://dx.doi.org/10.1016/j.compfluid.2005.02.011.
[86] Tayfun E. Tezduyar, Finite elements in fluids: special methods and enhanced solution techniques, Comput. & Fluids 36 (2) (2007) 207–223.
[87] Jonathan A. Dantzig, Michel Rappaz, Solidification: -Revised & Expanded, EPFL Press, 2016.
[88] Chen Ma, Dieter Bothe, Direct numerical simulation of thermocapillary flow based on the volume of fluid method, Int. J. Multiph. Flow. 37 (9) (2011) 1045–1058.
[89] S. Nas, G. Tryggvason, Thermocapillary interaction of two bubbles or drops, Int. J. Multiphase Flow 29 (7) (2003) 1117–1135.
[90] N.O. Young, J.S. Goldstein, Mi J. Block, The motion of bubbles in a vertical temperature gradient, J. Fluid Mech. 6 (3) (1959) 350–356.
[91] W. Pitscheneder, T. DebRoy, K. Mundra, R. Ebner, Role of sulfur and processing variables on the temporal evolution of weld pool geometry during multikilowatt laser beam welding of steels, Welding J. 75 (3) (1996) 71–81.
[92] P. Sahoo, T. DebRoy, M.J. McNallan, Surface tension of binary metalsurface active solute systems under conditions relevant to welding metallurgy, Metall. Mater. Trans. B 19 (3) (1988) 483–491.